

# **DESIGN AND TEST OF A BAT ROBOT**

A Thesis  
Presented to  
The Academic Faculty

By

Tao Song

In Partial Fulfillment  
of the Requirements for the Degree  
Master of Science in  
Mechanical Engineering

Georgia Institute of Technology

May 2020

Copyright © 2020 By Tao Song

# DESIGN AND TEST OF A BAT ROBOT

Approved by:

Dr. Seth A. Hutchinson, Advisor  
School of Interactive Computing  
*Georgia Institute of Technology*

Dr. Anirban Mazumdar  
School of Mechanical Engineering  
*Georgia Institute of Technology*

Dr. Oliver Sawodny  
Institute for System Dynamics  
*University of Stuttgart*

Dr. Cristina Tarin  
Institute for System Dynamics  
*University of Stuttgart*

Date Approved: March 26, 2020

## **ACKNOWLEDGEMENT**

I would like to express my deepest appreciation to my advisor, Dr. Seth Hutchinson, who has supported and funded this research work.

I would like to thank Johnathan Hoff, who helps me understand the state-of-the-art status of the B2 project based on which this work is conducted and helped me with the test of the new B2 robot.

## TABLE OF CONTENTS

ACKNOWLEDGEMENT .....	iii
LIST OF TABLES .....	v
LIST OF FIGURES .....	vi
SUMMARY .....	viii
Chapter 1 INTRODUCTION .....	1
Chapter 2 LITERATURE REVIEW .....	3
2.1 Aerodynamic Forces and Angles.....	3
2.2 Bat Wing Structure and Morphology.....	4
2.3 Flight Control .....	9
Chapter 3 DESIGN AND CONSTRUCTION.....	15
3.1 Design .....	15
3.2 Wing Motion .....	19
3.3 Construction .....	30
3.4 Electronics .....	35
Chapter 4 TESTS AND RESULTS.....	42
4.1 Load Cell Test .....	42
4.2 Flight Test.....	53
Chapter 5 CONCLUSION .....	61
REFERENCES.....	63

## LIST OF TABLES

Table 1: The length of each link.....	24
Table 2: Range of folding and bending angles.....	25
Table 3: Pulse-width modulation (PWM) input and corresponding output voltage .....	38
Table 4: Encoder positions and slave addresses.....	40
Table 5: Thrust and lift generated by B2 folding and bending wings .....	47
Table 6: Thrust and lift generated by B2 with fixed wings .....	51
Table 7: Roll and yaw moment .....	52

## LIST OF FIGURES

Figure 1: Basic aerodynamic forces [10] and angles [11] .....	4
Figure 2 [8]: Degrees of freedom on a bat wing .....	5
Figure 3 [13]: Bat wing morphologies of a) twisting, b) cambering, c) bending, d) wing-area changing, and e) flapping .....	5
Figure 4 [24]: Wing leading edge.....	9
Figure 5 [14]: Bat wing structure .....	10
Figure 6 [11]: Banked turn and crabbed turn .....	12
Figure 7 [35]: Construction of the bat robot designed by Festo .....	16
Figure 8 [7]: Wing structure without bending movement .....	17
Figure 9: New design of wing structure with a) isometric view, b) top view, and c) front view .....	18
Figure 10: Folding and bending angle versus spindle drive displacement .....	25
Figure 11: Flapping mechanism of B2 .....	26
Figure 12: Flapping angle over crank rotational angle.....	28
Figure 13: Construction of B2: with a) tail, b) bottom view, and c) isometric view .....	32
Figure 14: Schematics of the electronic parts .....	36
Figure 15: Thrust at 3Hz when both wings folded during the upstroke .....	44
Figure 16: Lift at 3Hz when both wings folded during the upstroke .....	44
Figure 17: Thrust at 4Hz when both wings folded during the upstroke .....	45
Figure 18: Lift at 4Hz when both wings folded during the upstroke .....	45
Figure 19: Thrust at 5Hz when both wings folded during the upstroke .....	45
Figure 20: Lift at 5Hz when both wings folded during the upstroke .....	46
Figure 21: Thrust at 6Hz when both wings folded during the upstroke .....	46
Figure 22: Lift at 6Hz when both wings folded during the upstroke .....	46

Figure 23: Thrust at 3Hz when both wings are fixed .....	48
Figure 24: Lift at 3Hz when both wings are fixed .....	49
Figure 25: Thrust at 4Hz when both wings are fixed .....	49
Figure 26: Lift at 4Hz when both wings are fixed .....	49
Figure 27: Thrust at 5Hz when both wings are fixed .....	50
Figure 28: Lift at 5Hz when both wings are fixed .....	50
Figure 29: Thrust at 6Hz when both wings are fixed .....	50
Figure 30: Lift at 6Hz when both wings are fixed .....	51
Figure 31: Thrust and lift at each frequency of fixed and folding wings .....	51
Figure 32 [36]: Indoor drone arena at the University of Illinois, Urbana-Champaign.....	53
Figure 33: Trajectory of the straight flight data in the x-y-plane.....	56
Figure 34: Euler angles of all straight flight tests .....	57
Figure 35: Trajectory of the turning flight data in the x-y plane .....	58
Figure 36: Euler angles of three turning flight tests .....	59

## SUMMARY

This thesis presents a new structure to improve the performance of a biologically inspired bat robot called Bat Bot (B2). In the previous work, a bat robot with five degrees of actuation was designed. This structure significantly simplified the morphology of a biological bat, which has over 40 degrees of freedom (DOFs), while still covering the most important DOFs for bat flight. In the present work, a new parallel structure is introduced to B2's wing to enable the distal part of the wings to bend downward and fold at the same time during the upstroke. Since this additional DOF is passive, no other actuator is required. The new generation of B2 has following DOFs: (1) synchronized wing flapping, (2) asynchronous folding and bending coupled by the new parallel structure, and (3) asynchronous dorsoventral movement of the hindlimbs.



## **Chapter 1**

### **INTRODUCTION**

In recent years, many efforts have been dedicated to designing and constructing biomimetic robots. Research on animal behavior can provide insight into the principles of its underlying mechanisms, which can be applied to engineering to build more powerful and functional robots. For example, fish can achieve higher propulsive efficiency and maneuverability compared to a conventional marine vehicle that is powered by propellers with same energy consumption [1]. [2] has developed gecko-inspired synthetic dry adhesives for wall-climbing robots, which can be used for inspection and cleaning.

Furthermore, studies have been performed to develop flying robots, such as SmartBird [3] by Festo. [4] has reported insect-like flapping wings for hovering, and [5] has designed flapping wings that are inspired by those of birds. Although bat flight has been studied for decades, the incorporation of the flight mechanism of a bat into a flying robot is challenging. Compared to an airplane or quadcopter, a bat wing has a more sophisticated structure with over 40 degrees of freedom (DOFs). This complicated morphological property allows a bat to vary its wing kinematics during one wingbeat cycle. Such flexibility provides the bat with significant agility. However, a biomimetic robot with equivalent DOFs would be too complicated to fly, and the actuators and structures that are required to fully achieve these DOFs would result in a robot that is too heavy to fly, as it could not produce sufficient lift to compensate for its own weight. Excessive degree of actuators (DOAs) would also lead to an overly complicated control system for autonomous flight. Hence, many studies [6] [7] [8] have been conducted to determine the most dominant DOFs of bat flight and simplify the design.

In the initial work of B2 [7], a mechanism with five DOAs was designed for the robot. This mechanism allows B2 to flap both wings synchronously while folding and unfolding each wing asynchronously. The hindlimbs are able to move dorsoventrally and are independent from wing flapping to stabilize the flight. Both wing flapping and each hindlimb movement has one DOF. The folding and unfolding motions of each wing couple three biologically meaningful movements: humeral retraction and protraction, elbow flexion and extension, and carpal abduction and adduction [9].

In the recent generation of B2 [7], the flapping and folding are coupled by a linkage mechanism such that this generation of B2 has only three DOAs, namely the synchronous flapping and folding and the independent dorsoventral movement of each hindlimb. Compared to the previous work, this design simplifies B2's structure and is capable of creating more lift, but it can also restrict B2's turning maneuver since both wings have the same kinematics at all times.

In this paper, a new design of B2 is introduced. This new structure enables the distal part of the wing to bend and fold simultaneously during the upstroke. A series of load cell and flight tests were conducted to demonstrate that this new structure can increase the lift generation without reducing the flight stability. Following this introduction, Chapter 2 summarizes morphological properties from studies on biological bats. Then, Chapter 3 presents the new B2 design based on the information in Chapter 2, and Chapter 4 details the test results. Finally, Chapter 5 presents the conclusion.

## **Chapter 2**

### **LITERATURE REVIEW**

This part of the thesis offers an introduction to bat flight. It starts with the basic aerodynamic concepts that relate to bat flight. Then, it summarizes the findings of state-of-the-art research on bat flight, including the elementary morphological properties of the wing as well as the maneuverability during flight. Based on this information, a new design of B2 is proposed in the next section with the aim of improving B2's flight performance.

#### **2.1 Aerodynamic Forces and Angles**

The four key forces for aerodynamics are lift, drag, thrust, and weight (see Figure 1). Thrust is parallel to the flight direction and points toward the bat's head. Drag occurs in the opposite direction of thrust. The net thrust is calculated by subtracting the drag from the thrust. A bat accelerates in the flight direction when the net thrust is positive and decelerates when the net force is negative. Similarly, lift and weight are in opposite directions, and both forces are perpendicular to the flight direction. They differ in terms of the net lift, as the bat ascends when the net lift is positive and descends when the net lift is negative.

The three angles for flight are roll, yaw, and pitch (see Figure 1). The roll axis is a longitudinal axis that originates at the center of gravity and is directed forward and parallel to the bat's body. The yaw axis is the vertical axis, which has its origin at the center of gravity and is directed toward the bottom of the bat's body. The pitch axis is a lateral axis that originates at the center of gravity and is directed to the side and parallel to the line from wingtip to wingtip.

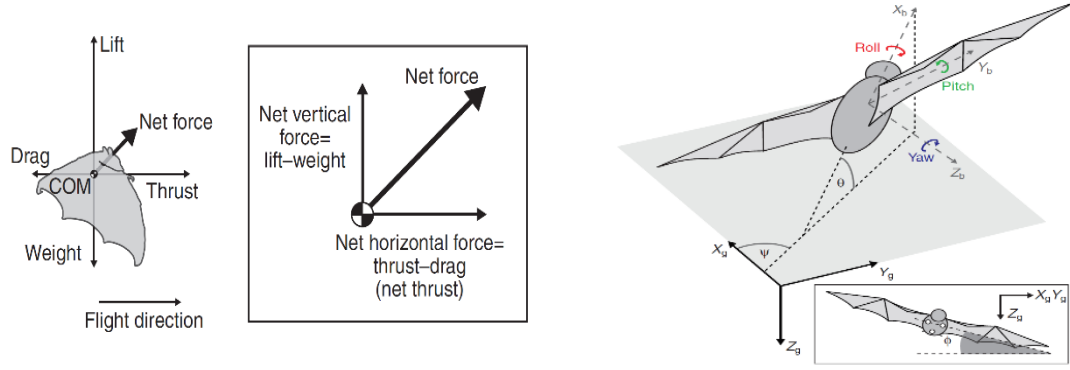


Figure 1: Basic aerodynamic forces [10] and angles [11]

## 2.2 Bat Wing Structure and Morphology

Over the last few decades, scientists have conducted extensive research on bat wing kinematics and aerodynamics to understand the high agility and maneuverability of bat flight. Compared to bird wings, bat wings have more DOFs beyond flapping and twisting (see Figure 2). Besides the dorsoventral movement and rotation, the humerus of a bat (joint c in Figure 2) can also retract and protract. This morphological property together with the elbow (joint d) flexion-extension and carpal abduction-adduction (joint e) enables the bat to fold its wings during the upstroke, which reduces the wing surface area. This kinematics can reduce the negative lift that is produced during the upstroke [12], which in turn increases the net lift that is generated during one wingbeat cycle.

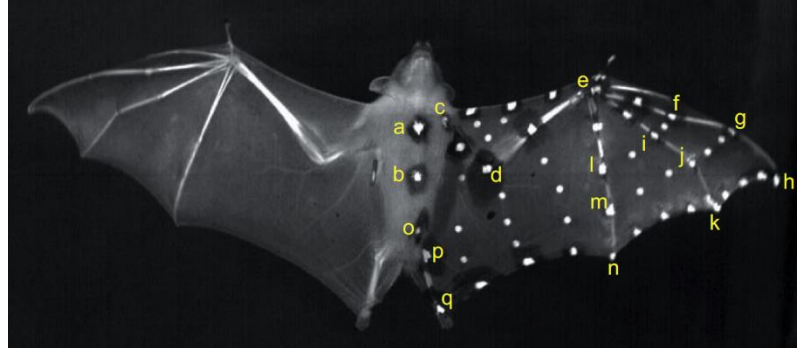


Figure 2 [8]: Degrees of freedom on a bat wing

At the distal part of the wing, a bat has five digits. Digit 1 is the thumb and has only one phalange. Depending on the species, digit 2 may or may not have a middle phalange between the metacarpal and distal phalange. Digit 3 (e-f-g-h), digit 4 (e-i-j-k), and digit 5 (e-l-m-n) have metacarpals, a middle phalange, and a distal phalange. The phalanges of the three long digits are able to flex and extend during flight, which contributes to the high maneuverability of bats. [13] has summarized the elementary morphological properties of a bat wing, which consist of cambering, bending, twisting, and wing-area changing (see Figure 3).

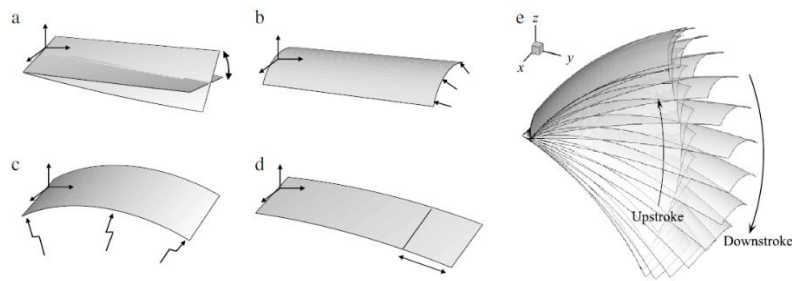


Figure 3 [13]: Bat wing morphologies of a) twisting, b) cambering, c) bending, d) wing-area changing, and e) flapping

Cambering is the anteroposterior wing deformation along the chordwise direction. Since bat wings have more DOFs than those of other flying animals, bat wings are capable of larger cambering [14]. Cambering can be controlled by bending digits and hindlimb movements. The body and leg movement determine the cambering near the body [14]. Increasing the leg angle ventrally relative to the body can heighten the leg-induced wing camber near the body [15]. At the midspan, cambering is mainly controlled by the downward flexion of the thumb and the fifth digit. At the distal part of the wing, it is controlled by the inclination of the dactylopatagium minus (deflection of the second digit) [16]. Hence, cambering varies at each chordwise cross-section along the wingspan.

In addition, cambering varies at each moment during one wingbeat cycle and is dependent on flight speed. [17] has indicated that cambering decreases as the flight speed increases. At the lowest flight speed of 1 m/s, the cambering at the mid-upstroke was about twice the cambering at the mid-downstroke. When the flight speed increased, cambering at both the mid-downstroke and mid-upstroke decreased. Cambering decreased significantly more at the mid-upstroke than at the mid-downstroke. Wing cambering is particularly important for slow flight, as it allows the wings to maximize lift at high AOA without stalling [18].

Bending refers to the wing deformation along the spanwise direction. Bats bend their wings more during the upstroke than during the downstroke. In addition, bats bend their wings while simultaneously retracting their upper limbs during the upstroke, which reduces the wing area [13]. During the downstroke, they stretch their upper limbs, which broadens the wingspan. The retraction or folding of the upper limbs is achieved by simultaneous humeral retraction, elbow flexion, and carpal abduction. During the downstroke, humeral

protraction, elbow extension, and carpal adduction allow the wingspan to be stretched (unfolding).

[19] has illustrated that folding the wing during the upstroke can reduce the cost of flapping by reducing the moment of inertia. Although wing folding and unfolding both require inertial energy consumption, which their experimental results indicate accounts for approximately 44% of the full inertial cost of flapping, the overall inertial energy cost is lower than it would be if the wings were to remain extended during the upstroke.

Twisting has been defined in [13] as the variation of the angle of attack (AOA) along the wingspan. Bat wings can undergo simultaneous flapping and spanwise twisting, which causes the magnitude of twisting to change along the wingspan and vary with the timing within one wingbeat cycle [20]. The morphological complexity allows the AOA to vary depending on the location of the wing and the timing.

Furthermore, [17] has supposed that wing twisting can contribute to the high values of mid-upstroke cambering at a low flight speed to permit the distal part of the wing to generate lift during the back-flick motion. It has been proven in [21] that the twisting of a bat wing has the functions of pronation and supination in insect flight, which can help a bat generate sufficient lift and thrust.

One special property of a bat is that the wing membrane is attached to not only the forelimbs but also the hindlimbs [22]. Hence, bat legs also have a role in the wing morphology and contribute to flight control. The hindlimbs of a bat are less complicated than the forelimbs. They undergo mostly dorsoventral and mediolateral movement, wherein the dorsoventral movement is dominant [6]. By testing a model with and without a tail membrane, [15] has determined that the change of pitch moment with increasing leg

angles was reduced when the tail membrane was absent. However, since there was little effect on the lift generation yet a significant increase in drag, they concluded that the hindlimb movement can potentially improve the agility and maneuverability by controlling the produced pitch moment and supporting the flight control. [23] has suggested that the amplitude of the hindlimb movement is most pronounced at the slowest flight speed, but a strong correlation between the amplitude of the hindlimb movement and the flight speed was not found in [22]. [22] has proposed that the hindlimb movement is not passively controlled by the tension in the wing membrane; instead, it is generated directly by muscle activity.

The AOA is the angle between the direction of air flow and the line that connects the leading edge and trailing edge of each chordwise cross-section of the bat wing. Due to wing twisting and cambering, the AOA of each chordwise cross-section varies along the wingspan. Increasing the angle of the legs relative to the body can also increase the AOA of the tail membrane [15]. The AOA is dependent on the flight speed. When the flight speed increases, the AOA decreases [17]. Because of the twisting and folding morphology of the bat wing, the AOA also varies for different parts of the wing and at different times during one wingbeat cycle. [17] has reported that the variation of the AOA along the spanwise direction of the wing was much higher during the upstroke than during the downstroke. Moreover, a lower flight speed led to a higher variation of the AOA compared to a higher flight speed. A negative AOA can be observed during the upstroke at the lowest flight speed since the air directly meets the upper surface of the wing during the wing's back-flick motion [17].



Although a larger AOA can increase lift, it also increases drag. When a critical AOA is exceeded, the airstream separates from the wing with a sudden fall in lift and increase in drag [16]. This phenomenon is called a “stall,” which results in a reduction of the lift-to-drag ratio and lift production [18].

## 2.3 Flight Control

### 2.3.1 Thrust and Lift in Low-speed Flight

Once the critical AOA has been reached, a further increase in the AOA no longer increases the lift-to-drag ratio, and stall occurs. However, bat is able to delay the stall with the leading-edge vortex (LEV). As Figure 4 demonstrates, the leading edge of a bat wing generates the LEV by separating the air that flows over the wing. However, the Kutta condition can be maintained if the separated airflow reattaches to the wing surface before reaching the trailing edge [24] [25]. Reattachment of the airflow is only possible for non-slender wings [26]. In a bat, the combination of the propatagium, the dactylopatagium brevis and minus, and the second and third phalange of the third digit function as the leading edge (see Figure 5). The leading-edge development of a bat relates closely to the cambering and shape-changing ability of a bat wing and can be created by lowering the thumb and the second digit [16].

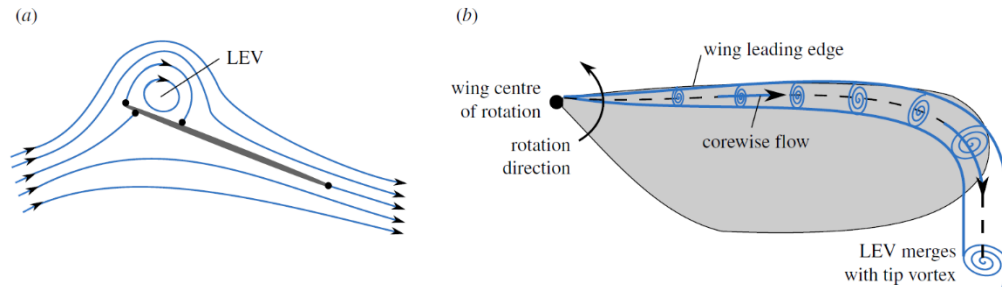


Figure 4 [24]: Wing leading edge

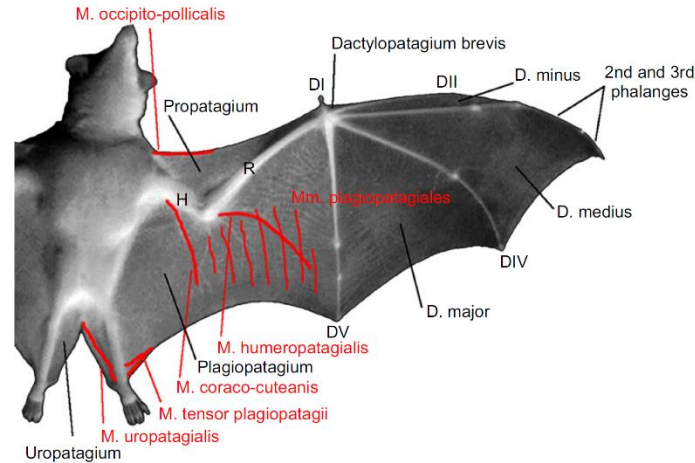


Figure 5 [14]: Bat wing structure

The LEV occurs when a bat is flying with a high AOA, which [14] has proven by illustrating the development of LEVs above the sharp leading-edge wings of bats when the AOA is sufficiently high. A small nectar-feeding bat can increase lift by 40% through the use of attached LEVs [27]. Because of the function of lift enhancement, the LEV is mostly present in low-speed flight, when the AOA and demands on lift are significant. [28] has indicated that the lesser-long nosed bat develops the LEV in slow forward flight at a high AOA, while the LEV is absent in higher-speed flight at a lower AOA. The effectiveness of the leading-edge flaps can be influenced by the leading-edge sharpness. Specifically, it increases with a decreasing leading-edge radius [16]. However, the high lift always comes at the cost of high drag that results in stall, even for leading-edge flapping.

Moreover, a bat is able to generate thrust in low-speed flight by using a tip-reversal or back-flip upstroke, whereby the distal part of the wing is moved upward and backward with respect to still air [10]. When the bat performs the tip-reversal upstroke, the armwings are highly flexed, while the handwings are fully extended and moved backward and upward as their ventral surfaces face upward and forward [29]. [30] has found that a backward and

upward flick of the wing at the end of the upstroke could probably generate thrust, and the bat would accelerate or maintain a constant speed. Meanwhile, the bat would slow down by using a vertical and reduced-span upstroke.

In regard to the reason for the thrust and lift generation during a tip-reversal upstroke, [20] has suggested two possible mechanisms by which the tip-reversal upstroke can generate thrust. In the first, the wingtip acts like a canoe paddle to push the air backward; in the second, the bat can likely over-supinate the wingtip to produce a positive AOA at the wingtip, which would allow lift to be produced locally. These two mechanisms are similar to those that have been proposed by [29]. Since the wings are accelerated backward and upward, the relative airflow directly meets the upper surface of the wings, which generates forward and upward lift as well as forward and downward drag. The resultant force can be separated into a forward thrust and a weight support, which correspond to the wingtip over-supination theory in [20]. Furthermore, a large drag force is generated as the wings are accelerated backward at the end of the upstroke. This force is directed forward and acts as thrust. This effect is similar to the effect that is described by the canoe paddle theory in [20].

### 2.3.2 Turning Maneuvers

Besides the lift and thrust generation during slow-speed flight and hovering, the super agility and maneuverability of turning maneuvers are also features of bat flight. The maneuverability varies between species of bats and depends on many factors. [31] has proposed that bats with long wings have a higher moment of inertia than those with short wings, and it is more difficult for them to initiate roll before turning since they need to generate more moment along their longitudinal axis. The study has also found that bats

with lower wing loadings could perform tighter maneuvers at a lower energetic cost. Therefore, a larger wing area with a shorter wingspan could improve maneuverability, which would imply that bats with wings of a higher aspect ratio have superior maneuverability.

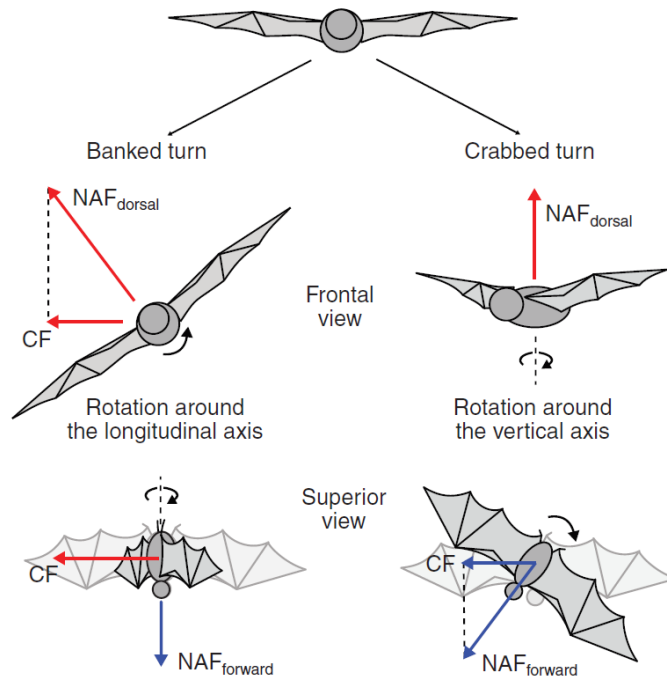


Figure 6 [11]: Banked turn and crabbed turn

In flying animals, the banked turn and crabbed turn in Figure 6 are most common [11]. A bat is able to use a combination of both types to make a turn. In a banked turn, the bat rolls into the turn. It tilts its body and banks its wings so that part of the net aerodynamic force in the dorsoventral direction that is generated during the downstroke can be used for lateral acceleration. Similarly, the bat yaws into the turn when performing a crabbed turn in order to accelerate laterally with the forward net aerodynamic force.

To perform a turning flight, a bat must generate different thrust, lift, or drag between two wings, which requires asymmetrical movement of both wings. [32] has indicated that a bat pronates (nose-down rotation of the wing about its spanwise axis) its inside wing and supinates (nose-up rotates) its outside wing to perform a roll without rotation in the yaw plane. The pronation of the inner wing decreases the AOA, while the supination of the outer wing increases the AOA and, hence, heightens the lift, which results in a roll toward the inner side.

Besides the asymmetrical twisting movement, the folding movement of both wings is asynchronized in the turning flight. During the second half of the downstroke, the inside wing begins to fold, while the outside wing remains outstretched. As a result, the outside wing generates more lift and thrust than the inside wing. During the second half of the upstroke, the outside wing remains folded as the inside starts to unfold. Therefore, more drag is generated on the inside wing than on the outside wing [11]. Because of the higher drag on the inside wing and higher lift on the outside wing, the bat gains lateral acceleration toward the inside wing.

To minimize the loss of overall energy during the turning flight, the bat changes its altitude while performing a turning maneuver. [33] has reported that a bat flew upward and gained height before turning; afterward, it made a 180-degree turn and dropped back down as it continued to fly in the opposite direction. Such ascension before turning and descension after turning have also been found in [31] and [34]. [34] has suggested that flying up while slowing down before the turn can transform kinetic energy into potential energy and thereby minimize the overall loss of mechanical energy. During the turn, the bat descends to convert potential energy into kinetic energy, which allows for maintaining or increasing

the speed. The descending action during the turn reveals that the bat is probably not able to produce sufficient lift to support its weight and balance the lateral acceleration at the same time, as the wing must be banked to produce lateral centripetal acceleration [34].

## **Chapter 3**

### **DESIGN AND CONSTRUCTION**

This chapter proposes a new structure of B2's wing on the basis of the summarized information in the previous chapter. This structure adds more morphological properties to the wing, which can improve B2's lift generation. In addition, the chapter describes the construction of B2, including the mechanical construction and electronic circuit building.

#### **3.1 Design**

In comparison to the previous wing structure, the structure of B2's wing in this work incorporates a linkage mechanism into the wing to add one passive DOF to each wing. As the previous chapter has explained, a bat is capable of bending its wings during the upstroke in addition to reducing the wing area by folding its wings. Since bending and folding both occur during the upstroke, these two morphological properties can be coupled. To this end, a mechanism is needed to transfer the linear motion of the spindle drive into the folding and bending of the wing at the same time.

Since the bending and folding have different rotation axes that are perpendicular to each other, bevel gears could be used at the wing carpal to transfer the carpal abduction and adduction into the bending of the distal part of the wing. However, the application of gears could complicate the wing structure as well as increase the weight of the distal part of the wing, which would heighten both the inertia of the outer wing and the energy consumption of the motor. The German company Festo has also developed a bionic flying fox [35] that has the ability to bend its wings during the upstroke. The bending movement in this robot is driven by a rack-and-pinion gear unit (see Figure 7). When the rack moves toward the

body of the robot, the distal part of the wing is pulled down. As a result, the wing bends. When the rack moves toward the far side of the wing, the distal part of the wing is pushed up, and the wing will be stretched. Even though this bending mechanism is independent of the folding and unfolding movement, the idea of bending the wing by pulling and pushing the distal part of the wing is feasible for the new design, which couples bending and folding.

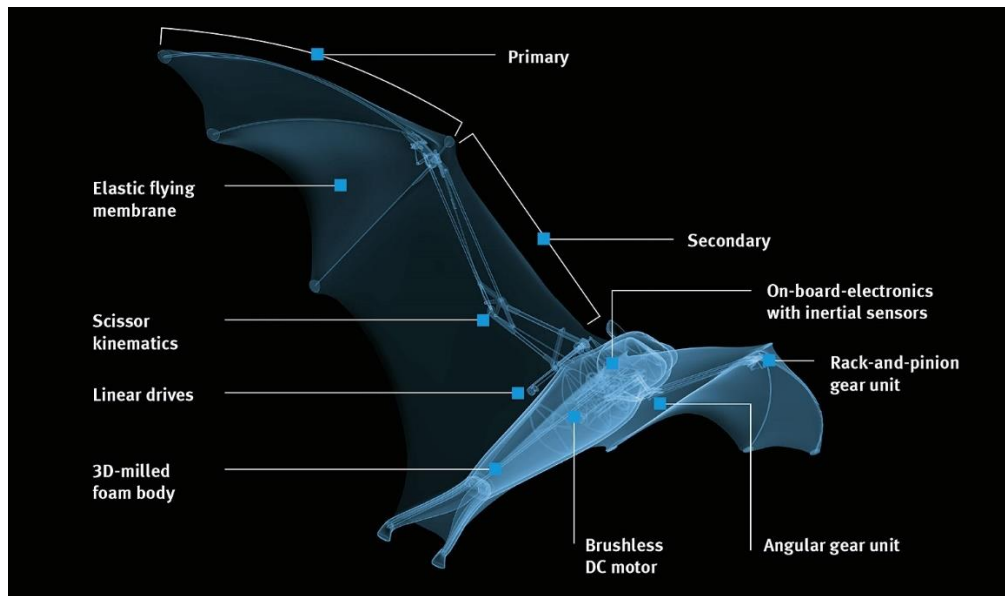


Figure 7 [35]: Construction of the bat robot designed by Festo

As Figure 8 illustrates, the distance between the joint  $p_6$  and any point on the carpal link (indicated by “c” in red) varies with the folding movement. When the wing folds, the distance lengthens; when the wing unfolds, it becomes shorter. This length variation can be utilized to drive the bending movement by incorporating an additional linkage mechanism between the radius link (indicated by “r” in red) and the radius support link (indicated by “rs” in red). Hence, an additional linkage is employed based on the previous design to pull and push the distal part of the wing.





connected to the carpal link. When the spindle drive moves linearly, the carpal plate moves together with carpal link, and the outer wing folds. At the same time, the carpal plate is pulled down by the second three-bar linkage, and the outer wing bends. Therefore, the new wing structure is able to fold and bend the wing at the same time.

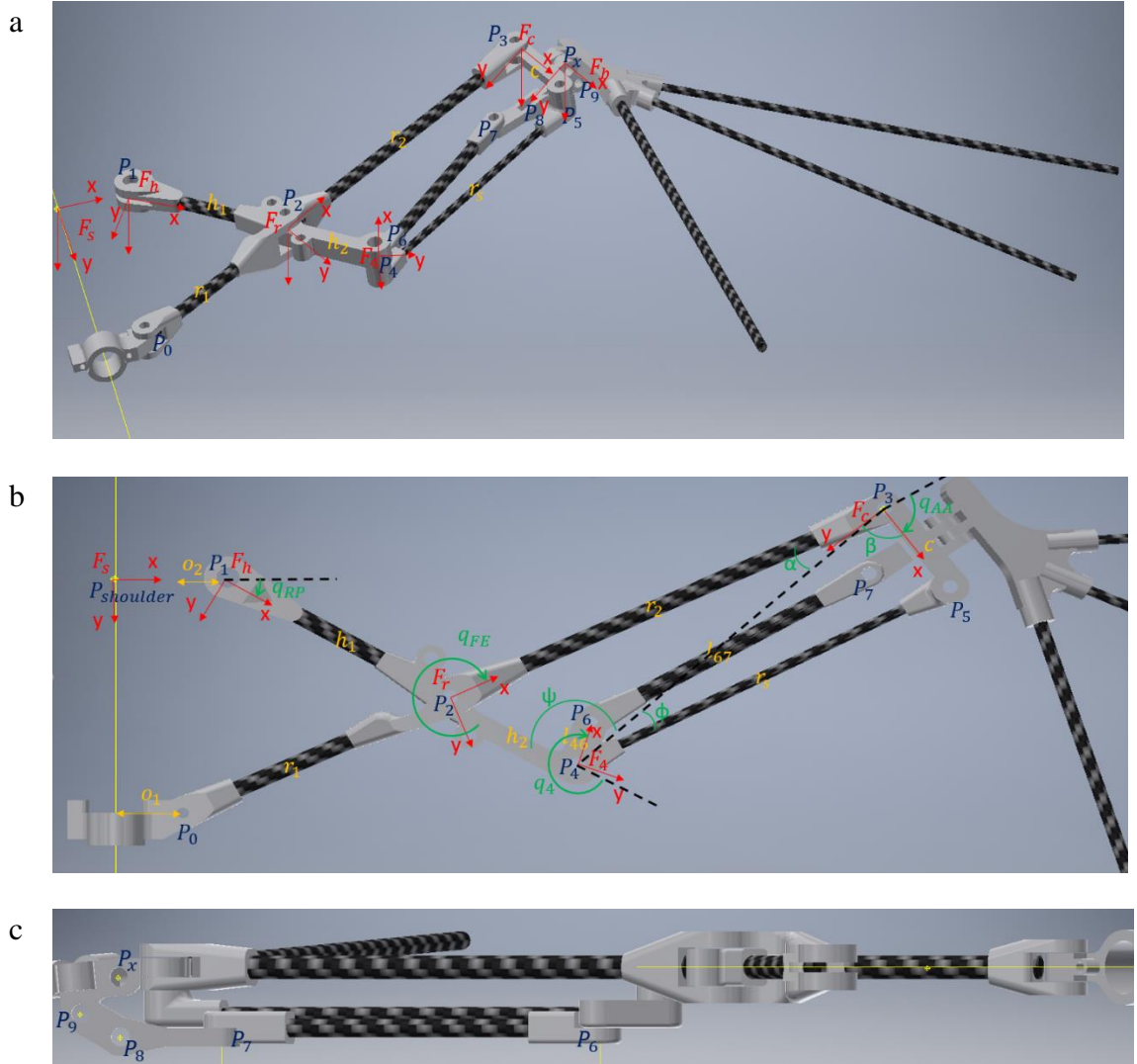


Figure 9: New design of wing structure with a) isometric view, b) top view, and c) front view

### 3.2 Wing Motion

To check B2's wing motion, four important wing angles (i.e. retraction-protraction, flexion-extension, abduction-adduction, and bending angle) and the coordinates of all joint points were computed in the shoulder coordinate system  $F_s$ . The shoulder coordinate system has its origin at the revolute shoulder joint. The y-axis is parallel to the body axis and points toward the tail. The x-axis is perpendicular to the y-axis in the wing plane and points toward the outer part of wing. The z-axis is determined by the right-hand rule and points into the face of the paper. Local coordinate systems were used to facilitate the calculation. The humeral coordinate system  $F_h$  has its origin at the revolute humeral joint  $P_1$ , and the x-axis is parallel to the humeral link. The radius coordinate system  $F_r$  has its origin at the revolute radial joint  $P_2$ , and its x-axis is parallel to the radius link. The carpal coordinate system  $F_c$  is located at the revolute carpal joint, and its x-axis is parallel to the carpal link. The z-axis of all coordinate systems points into the face of paper, and the y-axis is determined by the right-hand rule. Hence, the angle is positive when rotating in the clockwise direction. The transformation rotation matrix around the z-axis can be written as

$$R_z(q) = \begin{pmatrix} \cos(q) & -\sin(q) & 0 \\ \sin(q) & \cos(q) & 0 \\ 0 & 0 & 1 \end{pmatrix} \quad (1)$$

Before the coordinates of all joint points can be determined, all wing angles and their rotation matrix must be found. Since all wing DOFs are passive, and the angles are determined by the linear motion of the spindle drive, the relation between spindle position and wing angles must be determined.

As the spindle drive moves along the shoulder axis, the spindle position can be described in the shoulder coordinate system as  $(0, y_{sp}, 0)_{F_s}$ . As Figure 9 indicates, the wing plane

can be separately analyzed as a triangle  $p_0 - p_1 - p_2$  of the inner wing and a quadrilateral  $p_2 - p_3 - p_5 - p_4$  at the middle part of the wing. The retraction-protraction and the flexion-extension angle can be determined by the triangle of the inner wing.

Figure 9 also denotes the offset between  $p_0$  and  $p_1$  as  $o_2$ . Since the joint point  $p_0$  moves together with the spindle drive with an offset of  $o_1$ , its coordinate in shoulder frame can be described as  $(o_1, y_{sp}, 0)$ . Hence, the length of  $p_0 - p_1$  is  $\sqrt{o_2^2 + y_{sp}^2}$ . The skeleton  $h_1$  and  $r_1$  are fixed length, so all angles of the triangle can be determined. The retraction-protraction angle  $q_{RP}$  can be calculated as

$$q_{RP} = \pi - \arccos\left(\frac{h_1^2 + o_2^2 + y_{sp}^2 - r_1^2}{2h_1\sqrt{o_2^2 + y_{sp}^2}}\right) - \arctan\left(\frac{y_{sp}}{o_2}\right) \quad (2)$$

Although the angle  $p_0 - p_2 - p_1$  can be directly used as the flexion-extension angle  $q_{FE}$ , an obtuse angle in the clockwise direction as displayed in Figure 9 describes the angle  $q_{FE}$  for the convenience of calculation, as clockwise rotation is defined as positive. Therefore, the wrist angle  $q_{FE}$  is calculated as

$$q_{FE} = 2\pi - \arccos\left(\frac{h_1^2 + r_1^2 - (o_2^2 + y_{sp}^2)}{2h_1r_1}\right) \quad (3)$$

The abduction-adduction angle  $q_{AA}$  can be calculated by using the quadrilateral at the middle part of the wing. First, the length  $p_3 - p_4$  can be found in the triangle  $p_2 - p_3 - p_4$ . Then, the angles  $\alpha$  and  $\beta$  can be separately calculated in the triangles  $p_2 - p_3 - p_4$  and  $p_4 - p_3 - p_5$ , respectively. Finally, the abduction-adduction angle  $q_{AA}$  can be determined. The following equations describe the length  $p_3 - p_4$  and the angles  $\alpha$ ,  $\beta$ , and  $q_{AA}$ .

$$l_{34} = \sqrt{h_2^2 + r_2^2 - 2h_2r_2 \cos(q_{FE})} \quad (4)$$

$$\cos(2\pi - q_{FE}) = \cos(q_{FE}) = \frac{r_2^2 + h_2^2 - l_{34}^2}{2h_2r_2} \quad (5)$$

$$\alpha = \frac{r_2 - h_2 \cos(q_{FE})}{l_{34}} \quad (6)$$

$$\beta = \frac{l_{34}^2 + c^2 - r_s^2}{2cl_{34}} \quad (7)$$

$$q_{AA} = \pi - (\alpha + \beta) \quad (8)$$

By using  $q_{RP}$ ,  $q_{FE}$ , and  $q_{AA}$ , the coordinates of the joint points from  $p_0$  to  $p_5$  in the shoulder frame can be determined.  $p_0$  and  $p_1$  can be simply defined as

$$[p_0]_{F_s} = [o_1, y_{sp}, 0]_{F_s}^T \quad (9)$$

$$[p_1]_{F_s} = [o_1 + o_2, 0, 0]_{F_s}^T \quad (10)$$

The coordinate of joint points  $p_2$  and  $p_4$  can be easily found in the humeral frame and are  $[p_2]_{F_h} = [h_1, 0, 0]_{F_h}^T$  and  $[p_4]_{F_h} = [h_1 + h_2, 0, 0]_{F_h}^T$ . These coordinates can be transferred to the shoulder frame with help of the rotation matrix  $R_z(q_{RP})$ , so the coordinates of  $p_2$  and  $p_4$  in the shoulder frame can be calculated as

$$[p_2]_{F_s} = [p_1]_{F_s} + R_z(q_{RP})[p_2]_{F_h} \quad (11)$$

$$[p_4]_{F_s} = [p_1]_{F_s} + R_z(q_{RP})[p_4]_{F_h} \quad (12)$$

Similarly, the coordinate of joint point  $p_3$  in the radial frame can be described as  $[p_3]_{F_r} = [r_1, 0, 0]_{F_r}^T$ , and its coordinate in the shoulder frame can be calculated after two coordinate transformations.

$$[p_3]_{F_s} = [p_1]_{F_s} + R_z(q_{RP})\{[p_2]_{F_h} + R_z(q_{FE})[p_3]_{F_r}\} \quad (13)$$

Since the sum of the first two terms after the multiplication is equal to  $[p_2]_{F_s}$ , the coordinate  $[p_3]_{F_s}$  can be simplified as

$$[p_3]_{F_s} = [p_2]_{F_s} + R_z(q_{RP} + q_{FE})[p_3]_{F_r} \quad (14)$$

Finally, the coordinate of joint point  $p_5$  can be written as  $[p_5]_{F_c} = [c, 0, 0]_{F_c}^T$ , and its coordinate in shoulder frame can be obtained after three coordinate transformations.

$$[p_5]_{F_s} = [p_3]_{F_s} + R_z(q_{RP} + q_{FE} + q_{AA})[p_5]_{F_c} \quad (15)$$

Bending is a new feature in the new wing structure. As Figure 9a reveals, the carpal plane, which bends during folding, is connected to the carpal link such that it folds and bends at the same time. To achieve an easier calculation of the bending angle  $q_b$ , the bending angle is calculated in the carpal frame  $F_c$ . Hence, the coordinate of joint point  $p_4$  is transformed to the carpal frame.

$$[p_2]_{F_c} = [r_2 \cos(\pi - q_{AA}), r_2 \cos(\pi - q_{AA}), 0]_{F_c}^T \quad (16)$$

$$[p_4]_{F_c} = [p_2]_{F_c} + R_z(-q_{AA})[p_4]_{F_r} \quad (17)$$

To determine  $[p_6]_{F_c}$ , a coordinate frame  $F_4$  is defined at the joint  $p_4$ . The x-axis is parallel to the link  $p_4 - p_6$  and positive direction points from  $p_4$  to  $p_6$ . The z-axis is perpendicular to the wing plane and points downward. The y-axis is decided by the right-hand rule. Therefore, the coordinate  $[p_6]_{F_4}$  can be written as  $[l_{46}, 0, 0]_{F_4}^T$ . To transfer  $[p_6]_{F_4}$  to the carpal frame, rotation angle  $q_4$  must be found, which can be accomplished by using the quadrilateral at the middle part of the wing again. The calculation of  $q_4$  is similar to that of  $q_{AA}$ , in which the angles  $\varphi$  and  $\psi$  are separately calculated in two triangles. The angle offset of  $\alpha_o$  between  $p_4 - p_6$  and  $r_s$  should be subtracted from the result. Thus, angle  $q_4$  and  $[p_6]_{F_c}$  can be calculated as

$$q_4 = \pi + \arccos\left(\frac{l_{34}^2 + h_2^2 - r_2^2}{2h_2l_{34}}\right) + \arccos\left(\frac{r_s^2 + l_{34}^2 - c^2}{2r_sl_{34}}\right) - \alpha_o \quad (18)$$

$$[p_6]_{F_c} = [p_4]_{F_c} + R_z(q_4 - q_{FE} - q_{AA})[p_6]_{F_4} \quad (19)$$

As Figure 9c illustrates,  $p_7, p_8, p_9$ , and  $p_x$  are in same plane, as the rotational axes of joints  $p_8, p_9$ , and  $p_x$  are all parallel to the x-axis of the carpal frame. Joint  $p_x$  is fixed on the carpal plane, and its coordinate in the carpal frame is  $[p_x]_{F_c} = [7, -5, 1]_{F_c}^T$ . Therefore,  $[p_i]_{F_c}$  ( $i = 7, 8, 9, x$ ) can be written as  $[7, y_i, z_i]_{F_c}^T$ . Having already calculated  $[p_6]_{F_c}$ , and knowing the

length  $l_{67}$ ,  $y_7 = -\sqrt{l_{67}^2 - (7 - x_{p_6, F_c})^2} + y_{p_6, F_c}$  and  $y_8 = y_7 - l_{78}$  can be obtained and,

hence,  $[p_8]_{F_c} = [7, y_8, o_3]_{F_4}^T$ .  $o_3$  is the height offset between the original wing plane and the link  $p_7 - p_8$ . Having identified the coordinates of  $[p_8]_{F_c}$  and  $[p_x]_{F_c}$ , the length  $l_{8x}$  of the link  $p_8 - p_x$  can now be calculated.

Since points  $p_9$  and  $p_x$  are both fixed to the 3D-printed carpal plane part, the length  $l_{9x}$  of the link  $p_9 - p_x$  and its angle  $\gamma$  to the carpal plane are fixed values. With all of these values, it is finally possible to calculate the bending angle as

$$q_b = -\operatorname{atan}\left(\frac{z_{p_8, F_c} - z_{p_x, F_c}}{y_{p_8, F_c} - y_{p_x, F_c}}\right) - \operatorname{acos}\left(\frac{l_{8x}^2 + l_{9x}^2 - l_{89}^2}{2l_{8x}l_{9x}}\right) - \gamma, \quad \operatorname{atan}\left(\frac{z_{p_8, F_c} - z_{p_x, F_c}}{y_{p_8, F_c} - y_{p_x, F_c}}\right) < 0 \quad (20)$$

$$q_b = \pi - \operatorname{atan}\left(\frac{z_{p_8, F_c} - z_{p_x, F_c}}{y_{p_8, F_c} - y_{p_x, F_c}}\right) - \operatorname{acos}\left(\frac{l_{8x}^2 + l_{9x}^2 - l_{89}^2}{2l_{8x}l_{9x}}\right) - \gamma, \quad \operatorname{atan}\left(\frac{z_{p_8, F_c} - z_{p_x, F_c}}{y_{p_8, F_c} - y_{p_x, F_c}}\right) > 0 \quad (21)$$

After finding the bending angle, the coordinates of all digit ends can be calculated. A new coordinate system  $F_b$  is created at the bending joint. The direction of all axes of  $F_b$  is the same as that of those of  $F_c$ . The rotation at the bending joint occurs around the x-axis, and its rotational matrix is

$$R_x(q_b) = \begin{pmatrix} 1 & 0 & 0 \\ 0 & \cos(-q_b) & -\sin(-q_b) \\ 0 & \sin(-q_b) & \cos(-q_b) \end{pmatrix} \quad (22)$$

Here,  $-q_b$  is used as the rotation angle because the counterclockwise rotation around the x-axis (downward bending) is defined as the positive bending angle, while the clockwise rotation (upward bending) is considered negative. The coordinates of the digits' ends in the bending frame,  $[p_{d_3}]_{F_b}$ ,  $[p_{d_4}]_{F_b}$ , and  $[p_{d_5}]_{F_b}$ , are fixed values. Hence, their coordinates in the shoulder frame can be obtained by

$$[p_{d_i}]_{F_s} = [p_x]_{F_s} + R_z(q_{RP} + q_{FE} + q_{AA})R_x(q_b)[p_{d_i}]_{F_b}, i = 3,4,5 \quad (23)$$

$$[p_x]_{F_s} = [p_3]_{F_s} + R_z(q_{RP} + q_{FE} + q_{AA})[p_x]_{F_c} \quad (24)$$

By utilizing all of these equations, the range of  $\{q_{RP}, q_{FE}, q_{AA}, q_b\}$  during the wing-folding movement can be observed. The length of each link is originally set according to the values in Table 1.

Table 1: The length of each link

Link	Length[mm]	Link	Length[mm]	Link	Length[mm]
$\mathbf{o_1}$	9	$r_1$	40	$l_{67}$	43.5
$\mathbf{o_2}$	6	$r_2$	65	$l_{78}$	11
$\mathbf{o_3}$	7.5	$r_s$	57	$l_{89}$	5
$\mathbf{h_1}$	35	c	15	$l_{9x}$	$\sqrt{3.5^2 + 4.5^2}$
$\mathbf{h_2}$	20	$l_{46}$	7	$\alpha_o$	$\frac{\pi}{4}$

After inputting these equations and values in Matlab, the range of  $\{q_{RP}, q_{FE}, q_{AA}, q_b\}$  can be computed. The range of the spindle drive linear motion is set to  $[24mm, 45mm]$ . The computed result is presented in Figure 10. Apparently, as the spindle drive travels further away from the shoulder, the angles  $q_{RP}$ ,  $q_{FE}$ , and  $q_{AA}$  become smaller, which indicates that the wing is folding. At the same time, the bending angle  $q_b$  increases with the folding movement and can reach a maximum value of  $55.6^\circ$  when the wing is completely folded. The range of  $\{q_{RP}, q_{FE}, q_{AA}, q_b\}$  is displayed in Table 2. When the distance of the spindle drive motion is  $27\text{ mm}$ , the wing is fully extended. The range of retraction-protraction



angle is about  $20^\circ$ , while the range of flexion-extension and the abduction-adduction angle is about  $40^\circ$ . These ranges closely resemble the range of these three angles in a biological bat as noted in [7].

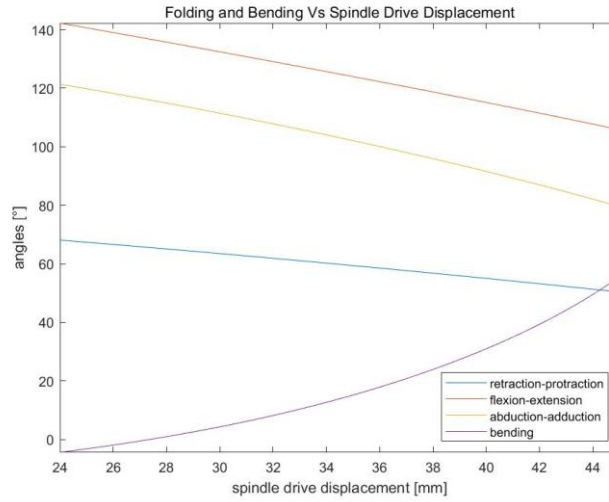


Figure 10: Folding and bending angle versus spindle drive displacement

Table 2: Range of folding and bending angles

	Minimum	Maximum	Range
$y_{sp}$	24mm	45mm	21mm
$q_{RP}$	$50.36^\circ$	$68.1^\circ$	$17.74^\circ$
$q_{FE}$	$105.83^\circ$	$142.22^\circ$	$36.39^\circ$
$q_{AA}$	$79.55^\circ$	$121.35^\circ$	$41.8^\circ$
$q_b$	$-4.4^\circ$	$55.6^\circ$	$60^\circ$

The coordinates of all important points can now be described in the shoulder frame. The last step is to transform them from the shoulder frame to the body frame. In this case, the flapping angle must be found. The flapping movement of B2 is controlled by a crank and

a ball-and-socket joint link. When the crank rotates, the ball-and-socket joint link pushes up or pulls down the shoulder of B2. For a more accurate review of the flapping angle range, the relationship between the crank angle and the flapping angle must be found.

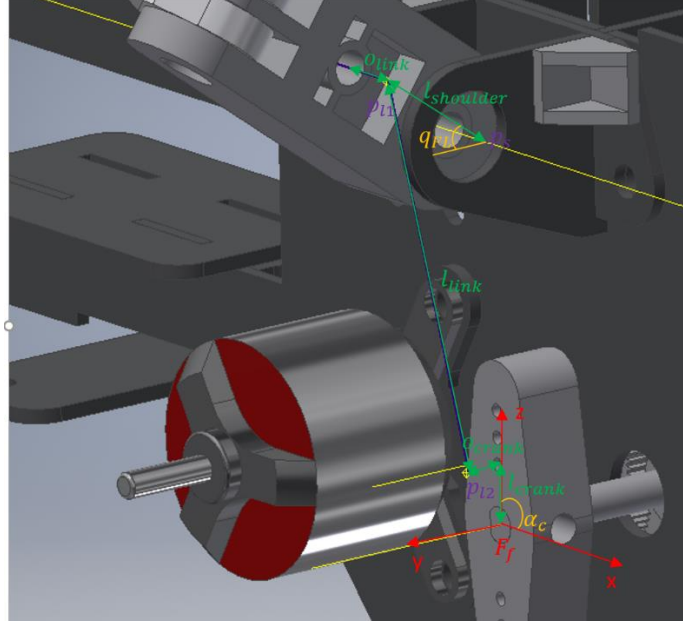


Figure 11: Flapping mechanism of B2

As Figure 11 demonstrates, the flapping coordinate system  $F_f$  is placed at the intersection of the crank surface and rotational axis. The z-axis is on the rotational axis and points outward. Meanwhile, the x-axis points toward the front of B2, and the y-axis points toward the top of B2. The range of the flapping angle is decided by the parameter  $\{l_{crank}, o_{crank}, l_{link}, o_{link}, l_{shoulder}\}$ . The parameter  $l_{shoulder}$  is a built-in length in the 3D-printed part. It is  $7.5mm$  and not adjustable. The adjustment of the two offset parameters  $o_{crank}$  and  $o_{link}$  does not significantly change the flapping range. However, some offset is necessary to ensure that the rotation of the ball-and-socket joint is not blocked by the crank or shoulder.

Finally,  $l_{crank}$  and  $l_{link}$  must be identified to establish the desired flapping range. The parameter  $l_{crank}$  determines the amplitude of the flapping angle, while  $l_{link}$  determines the offset of the flapping angle. The flapping amplitude increases alongside  $l_{crank}$ . A longer ball-and-socket joint link leads to a larger flapping angle in the upstroke, and a shorter ball-and-socket joint link produces a larger flapping angle in the downstroke.

In [7], the flapping angle of a biological bat during the upstroke reached about  $50^\circ$ , while the minimum angle during the downstroke was about  $55^\circ$ . In B2, the flapping angle reaches its maximum value when the projection of the ball-and-socket joint link on the x-z plane and the crank are parallel during the upstroke. The flapping angle reaches its minimum when they are parallel during the downstroke. Hence, the two parameters  $l_{crank}$  and  $l_{link}$  can be solved with two equations.

As Figure 11 indicates, the point of shoulder rotation is set to be  $p_s$  such that the link  $p_{l1} - p_{l2}$  is parallel to the shoulder. Since the coordinate of  $[p_s]_{F_f}$  in the flapping frame is  $[-1.15, -0.1, 21]^T$ ,  $[p_{l1}]_{F_f}$  can be written as

$$[p_{l1}]_{F_f} = [-1.15, -0.1 + l_{shoulder} \cdot \cos(q_{FL}), 21 + l_{shoulder} \cdot \sin(q_{FL})]_{F_f}^T \quad (25)$$

The coordinate of  $[p_{l2}]_{F_f}$  depends on the  $l_{crank}$  and is given as

$$[p_{l2}]_{F_f} = [l_{crank} \cdot \cos(\alpha_c), o_{crank}, l_{crank} \cdot \sin(\alpha_c)]_{F_f}^T \quad (26)$$

When the projection of the ball-and-socket joint link is parallel to the crank, the crank rotation angle that corresponds to the minimum and maximum flapping angle can be calculated simply by using the x- and z- components of  $[p_{l1}]_{F_f}$ .

$$\alpha_{c,q_{FL,max}} = \text{atan}\left(\frac{21 + l_{shoulder} \cdot \sin(q_{FL,max})}{-1.15}\right) + \pi \quad (27)$$

$$\alpha_{c,q_{FL,min}} = \text{atan}\left(\frac{21 + l_{shoulder} \cdot \sin(q_{FL,min})}{-1.15}\right) + 2\pi \quad (28)$$

Therefore, two equations with two unknown parameters  $l_{crank}$  and  $l_{link}$  are used.

$$\left\| [p_{l1}]_{F_f}(q_{FL,max}) - [p_{l2}]_{F_f}(\alpha_{c,q_{FL,max}}) \right\| = l_{link} \quad (29)$$

$$\left\| [p_{l1}]_{F_f}(q_{FL,min}) - [p_{l2}]_{F_f}(\alpha_{c,q_{FL,min}}) \right\| = l_{link} \quad (30)$$

Finally,  $l_{link} = 20.98mm$  and  $l_{crank} = 5.97mm$  are applied for a flapping range from  $-55^\circ$  to  $50^\circ$ .  $[-55^\circ, 50^\circ]$  is the flapping range of a biological bat in [7]. The next step is to calculate the flapping angle that corresponds to the crank rotational angle for the acquired parameters. To this end,  $[p_{l1}]_{F_f}$  is rewritten as  $[-1.15, y_{p_{l1}}, z_{p_{l1}}]_{F_f}^T$ . As in the previous calculation,  $y_{p_{l1}}$  and  $z_{p_{l1}}$  are solved by the following two equations.

$$\sqrt{(y_{p_{l1}} + 0.1)^2 + (z_{p_{l1}} - 21)^2} = l_{shoulder} \quad (31)$$

$$\sqrt{(-1.15 - l_{crank} \cdot \cos(\alpha_c))^2 + (y_{p_{l1}} - o_{crank})^2 + (z_{p_{l1}} - l_{crank} \cdot \sin(\alpha_c))^2} = l_{link} \quad (32)$$

Finally, the flapping angle  $\alpha_{fl}$  can be written as

$$q_{FL} = \text{atan}\left(\frac{z_{p_{l1}} - 21}{y_{p_{l1}} + 0.1}\right) \quad (33)$$

The result of the flapping angle over all crank angles is depicted in Figure 12.

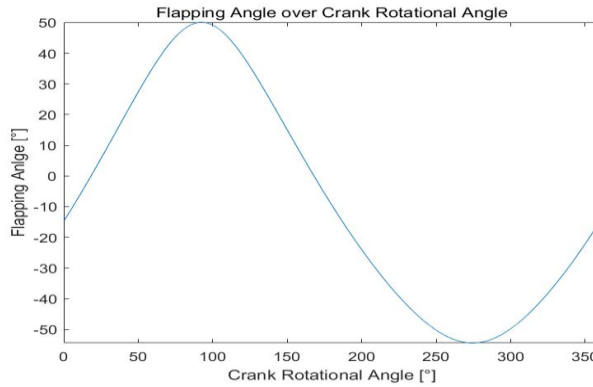


Figure 12: Flapping angle over crank rotational angle

After obtaining all biologically meaningful angles  $\{q_{RP}, q_{FE}, q_{AA}, q_b, q_{FL}\}$ , the coordinates of all of the joint points and digit ends can be transferred to the body frame. The origin of the frame  $F_{body}$  is located at the intersection of B2's middle plane, and the axis connects B2's two shoulder joints. The y-axis points toward the tail, while the x-axis points toward the lateral, and the z-axis points from the top of B2 to its bottom. The transformation matrix from  $F_s$  to  $F_{body}$  can be written as

$$R_y(q_{FL}) = \begin{pmatrix} \cos(q_{FL}) & 0 & \sin(q_{FL}) \\ 0 & 1 & 0 \\ -\sin(q_{FL}) & 0 & \cos(q_{FL}) \end{pmatrix} \quad (34)$$

In addition, the coordinates of all joint points and digit ends  $[p_i]_{F_{body}}$  can be calculated as

$$[p_i]_{F_{body}} = [p_{shoulder}]_{F_{body}} + R_y(q_{FL})[p_i]_{F_s}, i = 0, 1, \dots, 9, x, d_3, d_4, d_5 \quad (35)$$

### 3.3 Construction

Based on the design in the last chapter, a new bat robot was constructed (see Figure 13). For the construction of B2, materials of a low weight and high strength are preferred, as they can reduce weight of the robot. For this reason, carbon fiber was widely used for both the frame structure and the skeleton of B2. The body frames of B2 were formed from a 1/32-inch carbon fiber plate, and the wing skeletons and legs were created from hollow carbon fiber tubes. The carbon fiber plates were cut by a waterjet to obtain the required shapes, while the carbon fiber tubes were cut by a Dremel with a spinning disc to achieve the desired length.

The body frame of B2 consists of two carbon fiber frames that are 5 mm apart from each other. M2 screws were used to clamp the two carbon fiber frames, while several nylon spacers were placed between the two carbon fiber frames to ensure the distance between them. A brushless DC motor was laterally mounted on B2's body near its head to drive the flapping movement. The output torque of the brushless DC motor (BLDC) was increased by a factor of 30 through the use of a gear box with two gear stages. The BLDC was mounted onto the side of one carbon fiber frame by three M2 screws. Moreover, the pinion gear of the first gear stage was simply mounted onto the BLDC shaft through a press fit. No set screw or key was used for the connection.

The pinion gear of the second gear stage was inserted into the spur gear of the first gear stage. A hole was drilled into the spur gear that has the same shape as the pinion gear. Therefore, the spinning of the spur gear could be directly transferred to the pinion gear. A 1.5-mm stainless steel shaft was inserted into the pinion gear as the axis for these two gears. Furthermore, flanged sleeve bearings were applied on both sides to guide the shaft and

reduce friction during rotation. E-clips were employed to fasten the sleeve bearings, frame, and gears.

The joints of B2's wings and legs as well as the parts for mounting microactuators were 3D printed with selective laser sintering (SLS) nylon plastic. The SLS uses a laser as the power source for sintering powdered material to bind the material together and create a solid structure. This material has a low weight but can provide adequate strength. Each revolute wing joint was connected with M2 nylon screws, and the hollow carbon fiber tubes were inserted into the 3D-printed joints and glued with epoxy. To remove the carbon fiber tubes from the wing joints to perform any future modifications, a hot air gun can be utilized at about 150°C to heat and melt the epoxy. Since both SLS nylon and carbon fiber have a high melting point, heating the epoxy will not damage the other parts.

A titanium drive shaft is driven by the second spur gear, which was clamped by two 2-mm-thick Teflon plates to avoid axial movement along the drive shaft. To guide the drive shaft and reduce the friction during rotation, flanged bearings were inserted between the carbon fiber frame and drive shaft. One set screw shaft collar was applied on each side to fasten all of these components. In addition, one aluminum crank was mounted on each end of the drive shaft and fastened by a set screw. The aluminum cranks have multiple threaded M2 holes, each of which is a different distance from the rotational axis. Finally, a ball-and-socket joint link was used to connect the crank and wing, which converts the synchronous rotational movement of the cranks into the symmetric flapping of wings. The range of the flapping angles can be changed by adjusting the length of the ball-and-socket joint link as well as the distance between the threaded hole and the rotational axis on the crank.

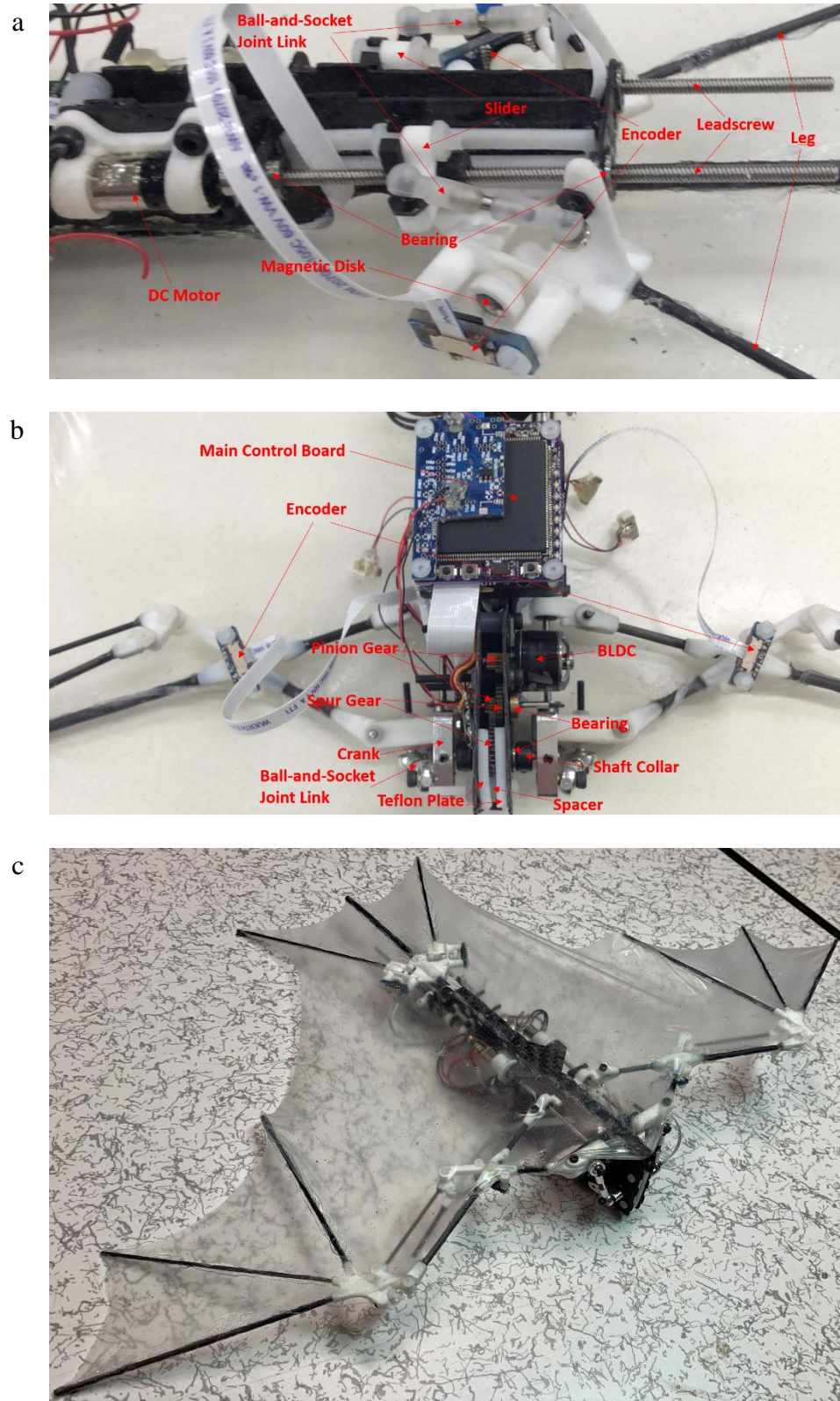


Figure 13: Construction of B2: with a) tail, b) bottom view, and c) isometric view



Both the wing's folding movement and hindlimb's dorsoventral movement are controlled by microactuators. These microactuators were inserted into the 3D-printed SLS nylon parts by a press fit, and the 3D-printed parts were mounted to the carbon fiber frames with M2 screws. A spindle drive was connected to each microactuator to transfer the rotational movement of the actuators into a linear movement that can directly drive the folding and unfolding movement of both wings. As for the hindlimb movement, a ball-and-socket joint link was employed on each side to transfer the linear movement of the spindle drive into the dorsoventral movement of the legs. The ball-and-socket joint link connects the slider on the spindle drive and part to hold the legs. Both sliders are comprised of 3D-printed SLS nylon plastic. As with the wing-flapping movement, the angle range of the dorsoventral movement can be adjusted by changing the length of the ball-and-socket joint link as well as the length of the crank. To reduce friction during sliding, Teflon plates were glued to the carbon fiber frames to guide the sliders.

To guide the spindle drives and reduce the friction during rotation, flanged bearings were inserted into the lateral frames, and epoxy was applied to hold the bearings in position. The lateral frames were inserted into the body frames and glued with epoxy. Furthermore, the aluminum frame brace was glued with epoxy to each corner between the body frame and lateral frame to prevent deformation of the lateral frames.

The membrane was the last part to be attached to B2 after all other parts, including the electronic parts, had been assembled. Platinum cure silicone was used to make the wing membrane. It consists of a two-component high tear strength and flexible mold or casting compounds: part A is a platinum catalyst, and part B is silicone hydride in combination with vinyl. Furthermore, a silicone solvent was added to the mixture to lower the viscosity

of the silicone rubbers. The proportion of the three parts in the mixture was 2:2:1. After the mixture was fully mixed, it was poured onto a 18"×12" polyester film, which was placed on a 18"×12" granite block. Then, another 18"×12" polyester film was placed on top. A scraper was used to evenly distribute the mixture from the middle to the left and right sides. During this process, all bubbles in the mixture had to be pushed out; otherwise, even tiny bubbles would become holes in the membrane once the solution had dried, which could reduce the strength of the membrane and render it useless.

The membrane should be very thin. After the solution was pushed evenly from the middle to the two sides, the remaining solution needed to be pushed off so that it spilled out from between the two polyester films. Finally, another 18"×12" granite block was placed on top to press the membrane. One clamp was used on each corner of the granite block to increase the pressure. The membrane must be pressed for at least 24 hours. Afterward, it was removed from the granite blocks while still covered by the polyester film, which made the cutting easier. Since polyester film can catch fire when it is cut by a laser, the membrane was cut to the desired form by hand.

The attachment of the membrane to B2 required caution and patience. After both polyester films had been removed, the membrane became highly elastic, which complicating the gluing step. Hence, only one polyester film was removed from the membrane. Then, the membrane was slowly and partially removed from the other polyester film until the removed part was large enough to be attached to the third digit of B2. The membrane was attached to the digit after silicone glue was coated on the carbon fiber tube. The membrane needed to be pressed by hand for a few minutes until the silicone glue dried; otherwise, the elasticity would cause the membrane to slip away from the digit.

### **3.4 Electronics**

B2's electronic circuit boards were originally designed in [6]. They were slightly modified and debugged for this thesis. The onboard avionics included a main control board, an interface board, an inertia measurement unit (IMU) board, five encoder boards, an electronic speed controller (ESC), and a receiver. Moreover, a debugging board was designed to debug the code. The schematic of the electronic circuit is provided in Figure 14. An E-flite 2S (7.4V) LiPo battery was used as the power supply. When the two-cell LiPo battery was fully charged, the voltage could reach 8.4V. The maximum current draw of the battery was 6.75A. The main control board carried the STM32F429IIT6 microprocessor and was powered directly by the LiPo battery. A voltage regulator was used to reduce the voltage to 3.3V to power the microprocessor. Both the interface board and the IMU board were connected to the main control board, which directly powered them.

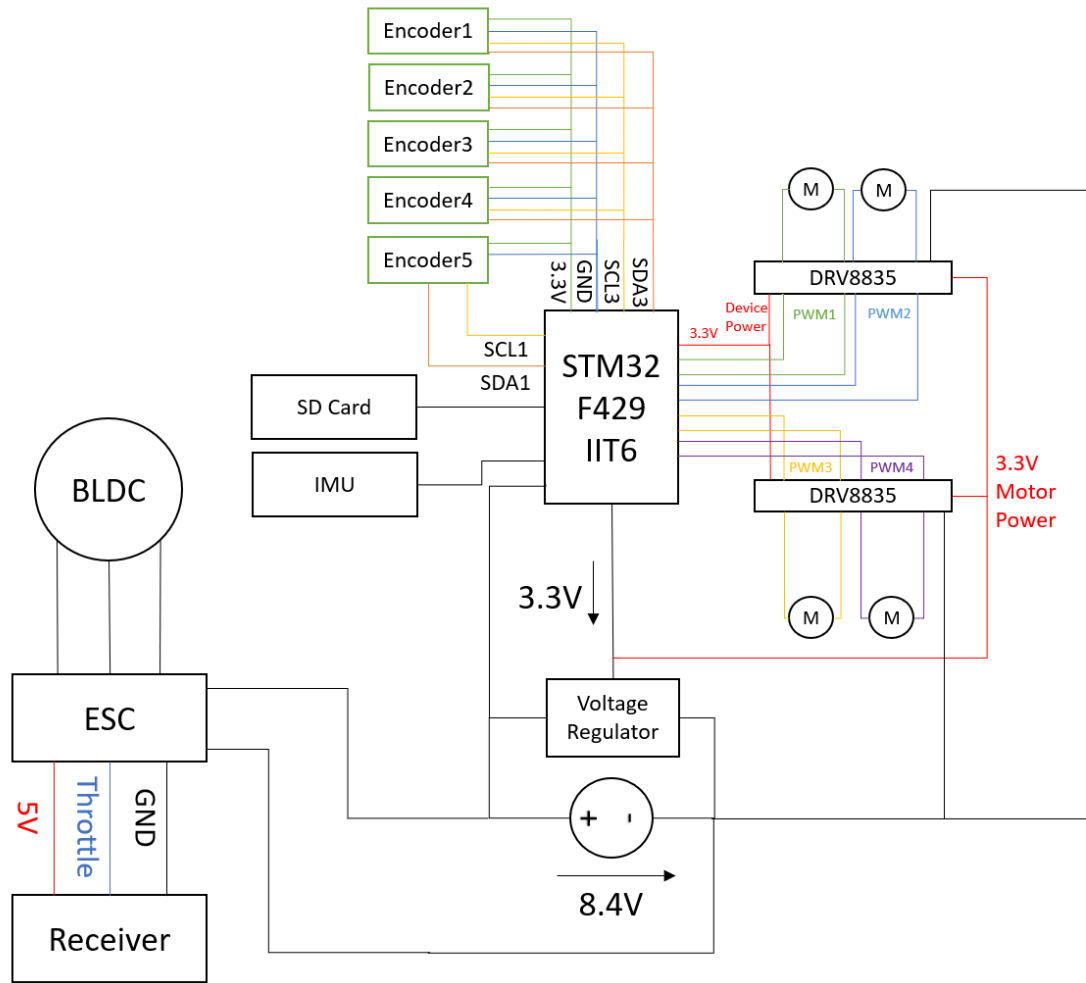


Figure 14: Schematics of the electronic parts

The interface board was connected to the main control board with an 18-pin ribbon cable, through which the microprocessor on the main control board sent four pairs of pulse-width modulation (PWM) voltages to the interface board. The interface board controlled four DC motors through the use of two DRV8835 H-bridge DC motor drivers. Each motor driver could control two DC motors with two pairs of PWM voltages. The DRV8835 motor driver required two power supplies: the device power supply and the motor power supply. The device power supply, which can range from 2V to 7V, was 3.3V in B2 and provided by the

main control board through a ribbon cable. This supply simply powered the driver and did not affect the voltage of the power supply to the DC motors. Meanwhile, the motor power supply can range from 2V to 11V and was independent of the device power supply. It drove the DC motors and was 3.3V in B2. The current of each DC motor could reach 150mA in operation, while the maximum allowable total current of the STM32F429IIT6 microprocessor was only 270mA. In addition, the microprocessor supported a high clock frequency of up to 168MHz, but the current consumption of the microprocessor itself could reach up to 100mA, even at room temperature. The DC motors cannot be powered by the main control board since the microprocessor turns off when the total current is continuously higher than 270mA. Therefore, all DC motors were powered directly by the 2S LiPo battery through another voltage regulator, which reduced the voltage to 3.3V. This voltage is slightly higher than the rated operation voltage of 3V. A 10 $\mu$ F capacitor was used to bypass the internal reference bypass pin of the voltage regulator to the ground, which reduced thermal noise on the output.

The DRV8835 motor driver had four input pins for receiving PWM voltages from the microprocessor as well as four output pins to output voltages to drive the DC motors. Every two input and output pins controlled one DC motor. The DRV8835 motor driver offers two operation modes: the PH/EN mode and the IN/IN mode. When the mode selection pin is connected to 3.3V, the motor driver operates in PH/EN mode. In the PH/EN mode, the PHASE pin controls the direction of the DC motor depending on whether the input is low or high. The ENABLE pin receives the PWM voltages and converts them linearly into output voltages to drive the DC motor.

The interface board of B2 uses the IN/IN mode, wherein the mode selection pin remains disconnected. The IN/IN mode is further divided into two operation methods: drive/coast and drive/brake. In the drive/coast operation, one input is set to be low (0V), and the other receives a PWM voltage. The output that corresponds to the low input is 0V. The other output should output a voltage of between 0V and 3.3V, which is linearly proportional to the duty cycle. The duty cycle ranges from 0 to 1. When the duty cycle is 0, the output voltage will be 0V. When it is 1, the output voltage will be 3.3V. However, testing indicated that the relationship between the output voltage and the input duty cycle is more logarithmic than linearly proportional in the drive/coast operation; therefore, B2 used the drive/brake operation. In this operation, one input was set to be high (3.3V), and the other received a PWM voltage. The output voltage that corresponded to the high input value is 0, while the other output outputs the voltage  $(1 - \text{duty cycle}) * 3.3V$ , where the duty cycle ranged from 0 to 1.

Table 3: Pulse-width modulation (PWM) input and corresponding output voltage

Input 1	Input 2	Output 1	Output 2	Operation
$PWM$	$0$	$PWM$	$0$	Forward speed at $PWM$ %
$0$	$PWM$	$0$	$PWM$	Reverse speed at $PWM$ %
$PWM$	$1$	$0$	$\overline{PWM}$	Forward speed at $(1-PWM)$ %
$1$	$PWM$	$\overline{PWM}$	$0$	Reverse speed at $(1-PWM)$ %

Besides driving the DC motors, the interface board also provided inter-integrated circuit (I2C) communication between the microprocessor and encoders. The interface board

carried four AS5048B magnetic rotary encoders on one I2C bus to read wrist and hip angles on both sides of B2. Each encoder on the same I2C bus must have a unique slave address, which was feasible with the AS5048B encoder because of the two address selection pins, A1 and A2. The slave address of the encoders contained seven bits, the five most significant of which were 10000. The two least significant bits were determined by pins A1 and A2. If A1 or A2 was connected to the ground, then the value of the corresponding bit was 0. If it was connected to 3.3V, then the value was 1. Hence, it was possible to have four different slave addresses and one for each encoder. The AS5048B encoder read the radius and hip angles by detecting the direction of magnetic field that surrounds it. A diametrically magnetized magnetic disk was attached to the wrist and the hip joint. When the magnetic disk rotated with a wrist or leg movement, the encoder could read the corresponding angle. An axially magnetized magnetic disk was not applicable here since the magnetic field did not change with the rotation along its axis.

In addition, one more encoder was needed to read the flapping angle. Since the flapping movement was designed to be synchronous, only one encoder was attached to the left shoulder of B2. Since no further slave address was available on the I2C3 bus on the interface board, this encoder was connected directly to the I2C1 (pin PB6 for SCL and PB7 for SDA) bus of the microprocessor on the main control board. Its slave address was set to 1000000. To ensure that the encoders would be stable during operation, the power supply needed to be either 3V or 5V. During the debugging, it was found that the encoders had become highly unstable, and the reading was inaccurate when the power supply dropped below 2.7V.

Table 4: Encoder positions and slave addresses

Encoder	Position	I2C Bus	SCL	SDA	Slave Address
Encoder 1	Right wrist	I2C3	PH7	PH8	1000000
Encoder 2	Left wrist	I2C3	PH7	PH8	1000001
Encoder 3	Right hip	I2C3	PH7	PH8	1000010
Encoder 4	Left hip	I2C3	PH7	PH8	1000011
Encoder 5	Shoulder	I2C1	PB6	PB7	1000000

The flapping movement of B2 was controlled by a Spektrum DX6e transmitter, a DELTANG DT RX31-F receiver, and a Thunderbird 6A brushless ESC. The three power cables of the brushless ESC were connected to the three phases of the brushless DC motor as well as the receiver. The brushless ESC was powered directly by the 2S LiPo battery. The ESC powered the receiver and was connected to its throttle channel. The receiver received the throttle signal from a Spektrum DX6e transmitter and sent the signal to the brushless ESC, which controlled the motor speed. After the receiver was connected to the LiPo battery, it beeped twice, which represented that it is a two-cell LiPo battery. The receiver was in scan mode when the light-emitting diode (LED) on the receiver flashed every two seconds. During binding with the transmitter, the LED flashed rapidly. After the receiver and the transmitter were bound, a series of beeps occurred, and the LED remained constantly on if the signal was good. Before binding, the throttle stick on the transmitter must be pulled down to avoid any accidents.

To collect flight data, the VectorNav VN-100S IMU was used. It was soldered onto the IMU board, which was connected to the main control board. A secure digital (SD) card



was inserted into the SD card slot of the IMU board to record the flight data that were collected by the IMU during the test flight. The IMU used SPI communication and was able to read roll, pitch, and yaw orientation angles of B2 during flight. In addition, it could record acceleration, quaternion, and gyro rates. Data that were collected by the IMU and encoders were employed for analysis of the flight results.

All electronic parts were mounted on B2 after they were debugged. Since the cable for B2 is very thin, it can break easily at the soldering position. Therefore, hot glue was used to increase the strength and prevent wire breakage. The interface board was placed between the two carbon fiber frames and fastened onto B2 with two M2 screws. The encoders were placed directly below or in front of the magnets at the wrist and hip joints. Each encoder was fastened to the 3D-printed parts with two M2 screws, and the IMU board and main control board were screwed together with M2 screws as well. The IMU board was placed between the main control board and B2 to protect it from damage when B2 fell onto the ground in the flight test. The receiver was glued to the outside of the left frame with hot glue, while the ESC was glued to B2's underside. The battery was placed near the tail.

## Chapter 4

### TESTS AND RESULTS

To validate the new design of the wing structure, B2 underwent several tests. First, a load cell test was conducted to measure the thrust and lift that were created by the new wing structure as well as the fixed wing without folding and bending. This experiment was intended to illustrate that the bending and folding movements during the upstroke generate more lift compared to the fixed wing. In addition, both lift and thrust were assumed to increase alongside the flapping frequency. The second experiment consisted of flight testing, including a straight flight test and a turning flight test. Both wings folded and bended during the upstroke in the straight flight test, while the left wing was fixed for the turning maneuver. This chapter details and validates the test results.

Since the DC motors that were used for B2 were not strong enough to make the folding and bending movement as fast as the flapping, the new wing structure was mounted to the robot in [7], which couples the flapping and folding movement, before commencing the test. In this way, B2 could fold and bend as quickly as it flapped.

#### 4.1 Load Cell Test

The setup of the load cell test was identical to that in [7]. B2 was mounted on a six-axis load cell, which measured force and torque in three directions. The x-axis pointed toward B2's head. The force  $F_x$  measure in this direction represented thrust, and the torque  $M_x$  around x-axis signified B2's roll. The z-axis pointed upward. Force  $F_z$  measured in this direction was lift, and torque  $M_z$  around the z-axis determined B2's yaw. The y-axis was determined by the right-hand rule. Torque  $M_y$  around this axis established B2's pitch. The signal of the load cell was recorded by a dSPACE box. A carbon fiber rod was inserted

into B2 beneath and parallel to the tailboom such that B2 could be mounted to the stand on the load cell. B2 was powered by a fixed power supply of 8.4V to drive the BLDC. The sampling frequency was 1,000Hz, and each test lasted for two seconds.

The experiment was conducted at four frequencies: 3Hz, 4Hz, 5Hz, and 6Hz. At each frequency, thrust and lift were recorded for fixed wings as well as the new wing structure. Tests were run three times for each of these eight settings, and the collected data were averaged. Because of B2's weight, the load cell performed readings even when the robot was not moving. Therefore, baseline data were collected each time once the robot had been mounted to the load cell. The averaged values of the baseline data were subtracted from the force and torque that were recorded in the tests.

The wing structure that featured folding and bending was tested first. The flapping frequency started at 3Hz and increased gradually to 6Hz. The collected thrust  $F_x$  and lift  $F_z$  data were processed after the test. The processed data are presented from Figure 15 to Figure 22. These figures reflect only three wingbeat cycles, although all completed wingbeat cycles of recorded data were employed to calculate the average thrust and lift. Table 5 displays the computed thrust and lift of each test run as well as the average thrust and lift at each frequency.

At the frequency of 3Hz, both generated thrust and lift were low. The thrust was 0.0073 *N*, 0.0113 *N*, and 0.0126 *N* in the three test runs, respectively. These figures result in an average thrust of 0.0104 *N* at the frequency of 3Hz. Meanwhile, the lift was 0.0113 *N*, 0.0119 *N*, and 0.0185 *N* in the three test runs, respectively. The average lift at 3Hz was 0.0139 *N*. When the flapping frequency was increased to 6Hz, the thrust increased to 0.0908 *N*, 0.0931 *N*, and 0.0917 *N* in the three test runs, respectively, which resulted in

an average thrust of  $0.0919\text{ N}$ . The lift also increased to  $0.0611\text{ N}$ ,  $0.0498\text{ N}$ , and  $0.0647\text{ N}$  in the three tests. The average lift at  $6\text{ Hz}$  was  $0.0585\text{ N}$ . At the frequency of  $6\text{ Hz}$ , the thrust increased by  $784\%$ , and the lift increased by  $320\%$  in comparison to the values that were recorded at  $3\text{ Hz}$ . As Table 5 reveals, both thrust and lift increased gradually with a higher frequency, which implies that the bat could generate more thrust and lift as it flapped more rapidly.

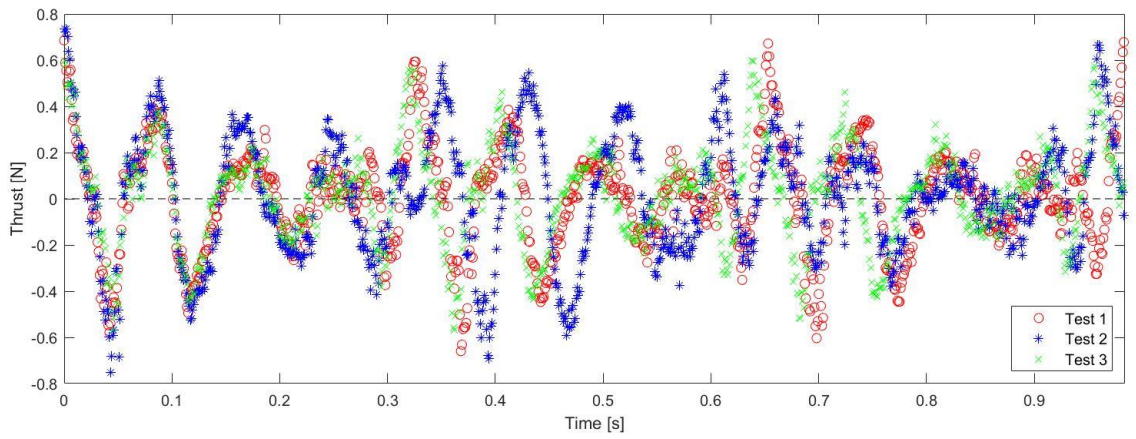


Figure 15: Thrust at  $3\text{ Hz}$  when both wings folded during the upstroke

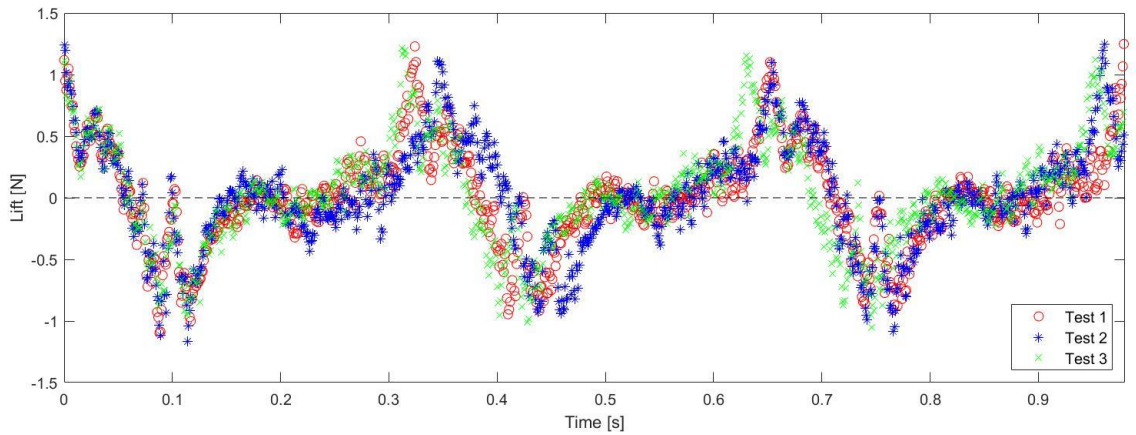


Figure 16: Lift at  $3\text{ Hz}$  when both wings folded during the upstroke

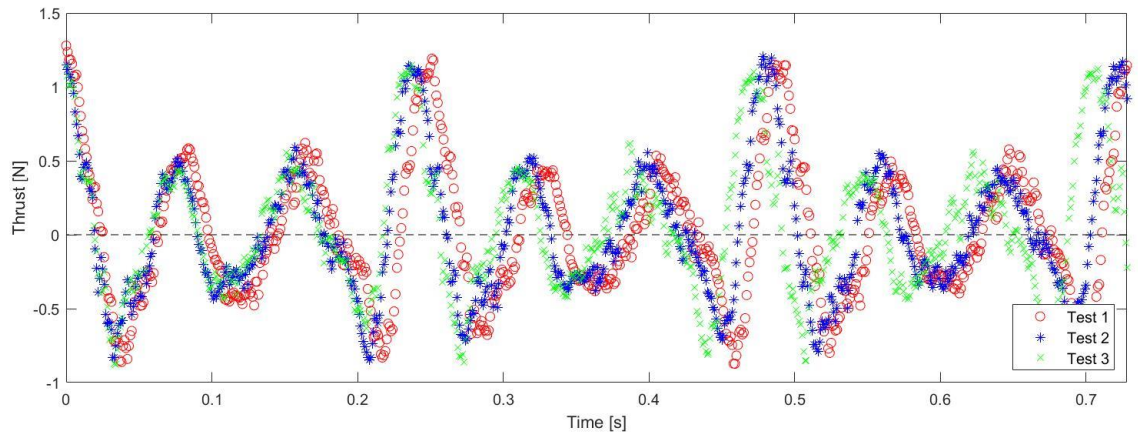


Figure 17: Thrust at 4Hz when both wings folded during the upstroke

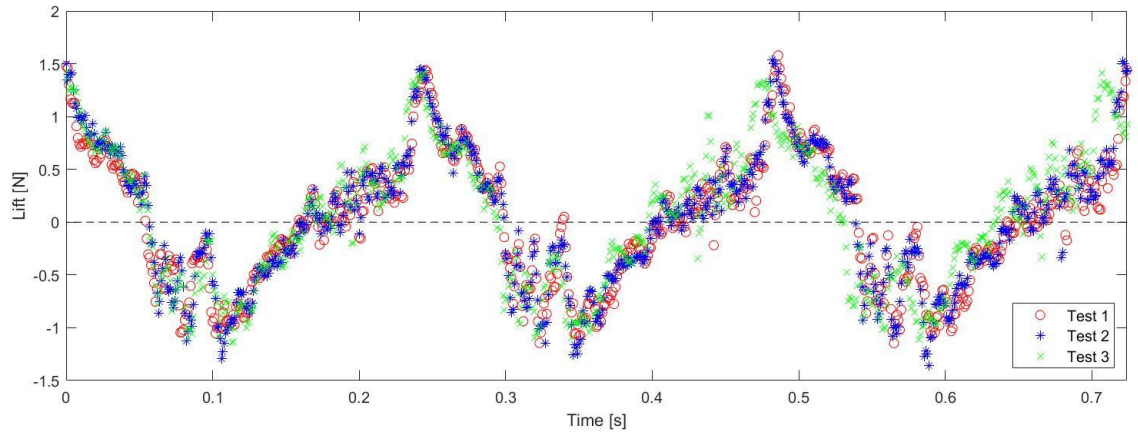


Figure 18: Lift at 4Hz when both wings folded during the upstroke

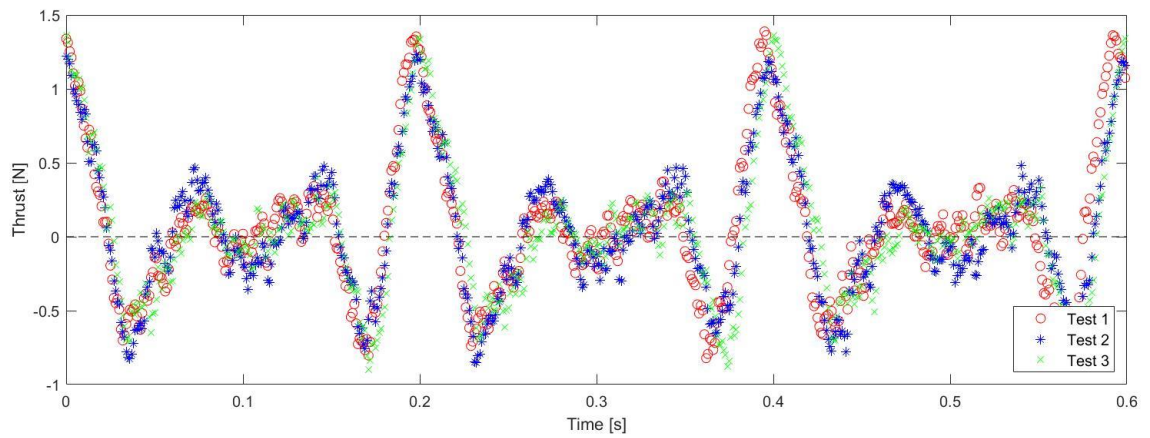


Figure 19: Thrust at 5Hz when both wings folded during the upstroke

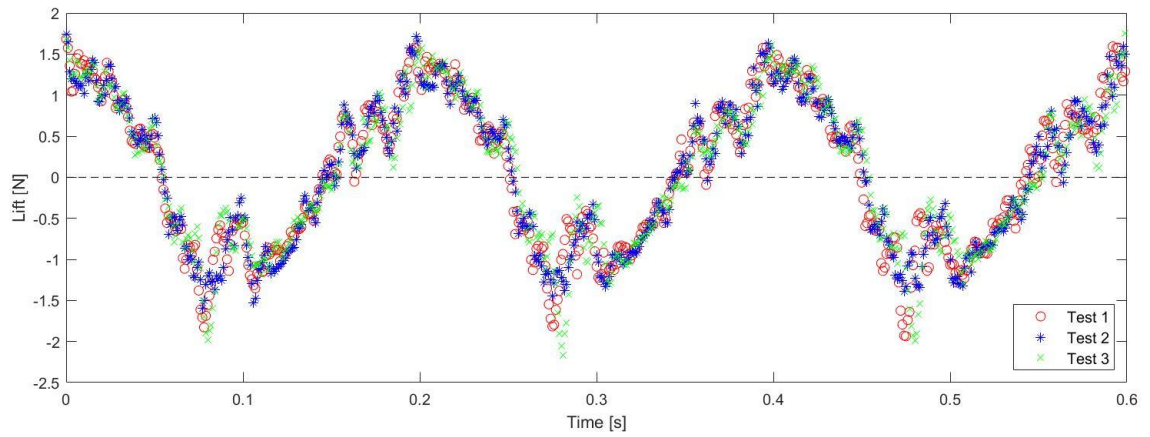


Figure 20: Lift at 5Hz when both wings folded during the upstroke

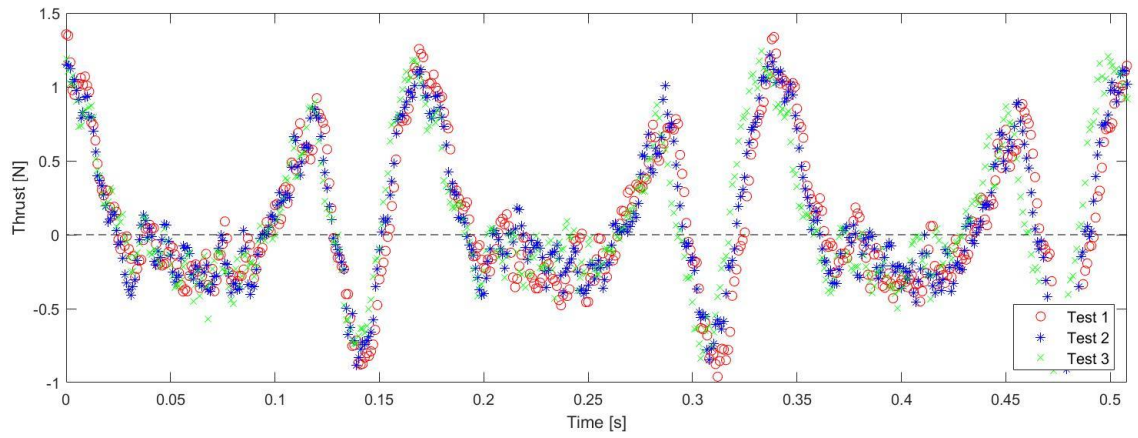


Figure 21: Thrust at 6Hz when both wings folded during the upstroke

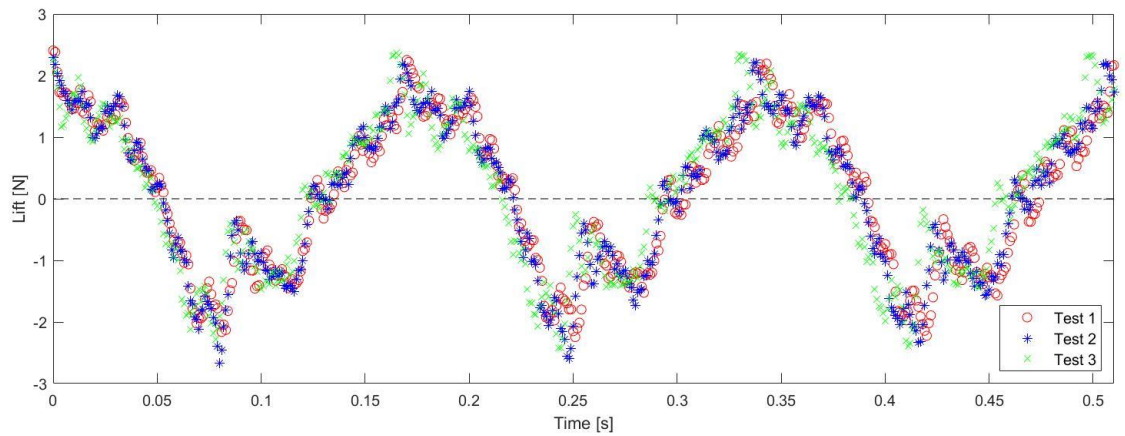


Figure 22: Lift at 6Hz when both wings folded during the upstroke

Table 5: Thrust and lift generated by B2 folding and bending wings

Force	Frequency	Test 1	Test 2	Test 3	Average
Thrust	3 Hz	0.0073 N	0.0113 N	0.0126 N	0.0104 N
	4 Hz	0.0244 N	0.0294 N	0.0361 N	0.0300 N
	5 Hz	0.0498 N	0.0501N	0.0501N	0.0500 N
	6 Hz	0.0908 N	0.0931 N	0.0917 N	0.0919 N
Lift	3 Hz	0.0113 N	0.0119 N	0.0185 N	0.0139 N
	4 Hz	0.0259 N	0.0331 N	0.0324 N	0.0304 N
	5 Hz	0.0342 N	0.0460 N	0.0517 N	0.0440 N
	6 Hz	0.0611 N	0.0498 N	0.0647 N	0.0585 N

To validate the potential of the new wing structure to provide superior performance, the same experiment was conducted on B2 with fixed wings. In this test, the wings did not fold or bend during the upstroke. Three tests were performed at every frequency from 3Hz to 6Hz. The trimmed data of these tests are presented from Figure 23 to Figure 30. Table 6 contains the computed thrust and lift in each test as well as the average thrust and lift. When both wings were fixed, the recorded thrust at 3Hz was 0.0178 N, 0.0208 N, and 0.0174 N. The averaged thrust at 3Hz was 0.0186 N. The recorded lift at 3Hz was 0.0024 N, 0.0030 N, and 0.0028 N. These figures result in an average lift of 0.0027 N at 3Hz for fixed wings. When comparing the thrust and lift at 3Hz between the fixed wing and the new wing structure, the new wing structure achieved a 415% increase in lift. However, it generated 44% less thrust compared to the fixed wing. At the frequency of 6Hz, the thrust that was produced by the fixed wing was 0.1826 N, 0.1885 N, and 0.1887 N. The average thrust was 0.1866 N at 6Hz for the fixed wing. In addition, the lift that was generated by the fixed wing at 6Hz was 0.0070 N, 0.0171 N, and 0.0145 N, which resulted in an average lift of 0.0129 N at 6Hz for the fixed wing. Hence, the fixed wing provided 903% more thrust and 378% more lift at 6Hz than at 3Hz. Faster flapping of the fixed wing also provided higher thrust and lift than the folding and bending wing achieved. Based on a



comparison of thrust and lift that were generated by the fixed wing and the new wing structure at 6Hz, the new wing structure was able to provide 353% more lift than the fixed wing; however, it reduced thrust by 50%.

As Figure 31 illustrates, B2 can clearly offer more lift when the wings fold and bend during the upstroke, but more thrust can be generated by the fixed wing. However, the lift enhancement of the new wing structure significantly exceeds the loss of thrust. Moreover, B2 must first be able to generate enough lift to maintain a long-term flight; otherwise, it will lose height quickly and land on the ground.

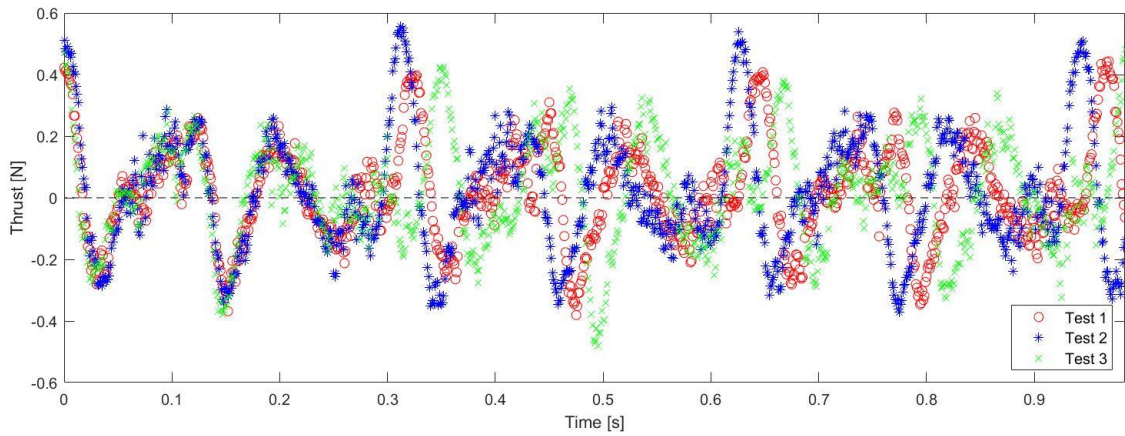


Figure 23: Thrust at 3Hz when both wings are fixed



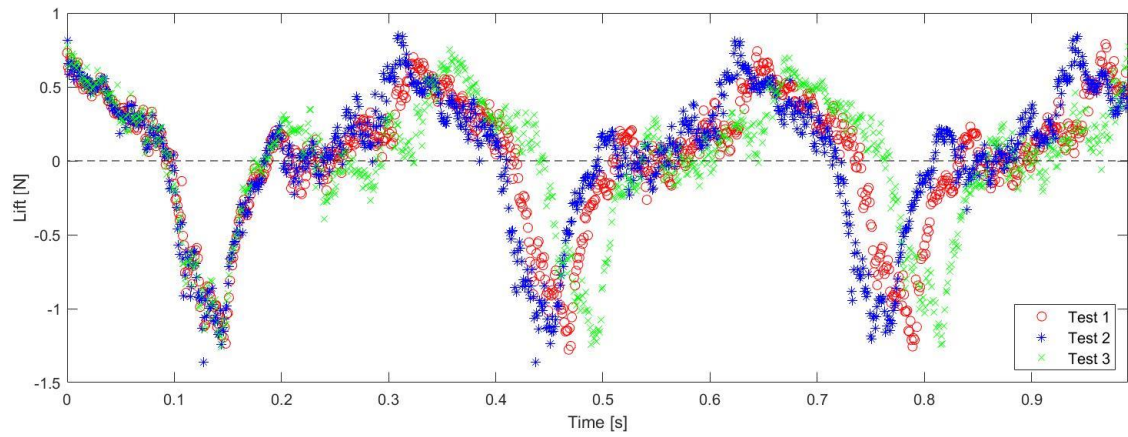


Figure 24: Lift at 3Hz when both wings are fixed

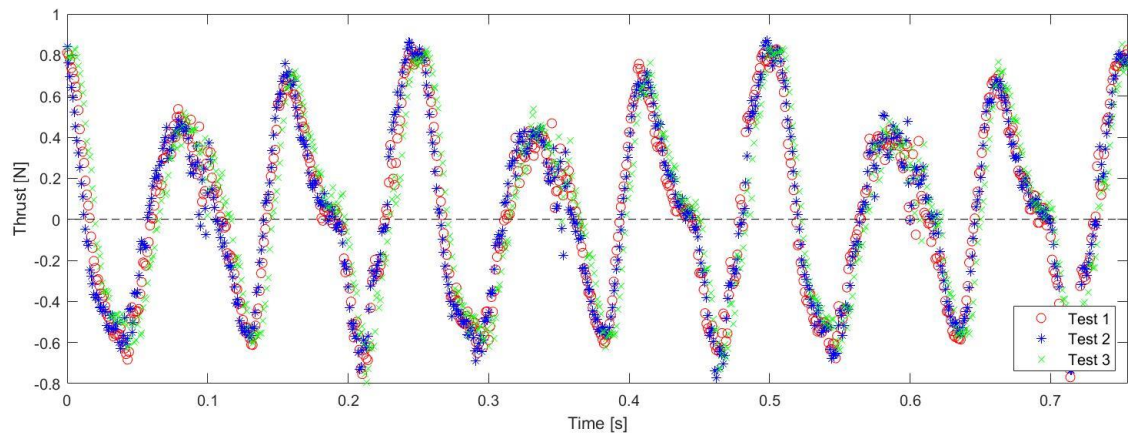


Figure 25: Thrust at 4Hz when both wings are fixed

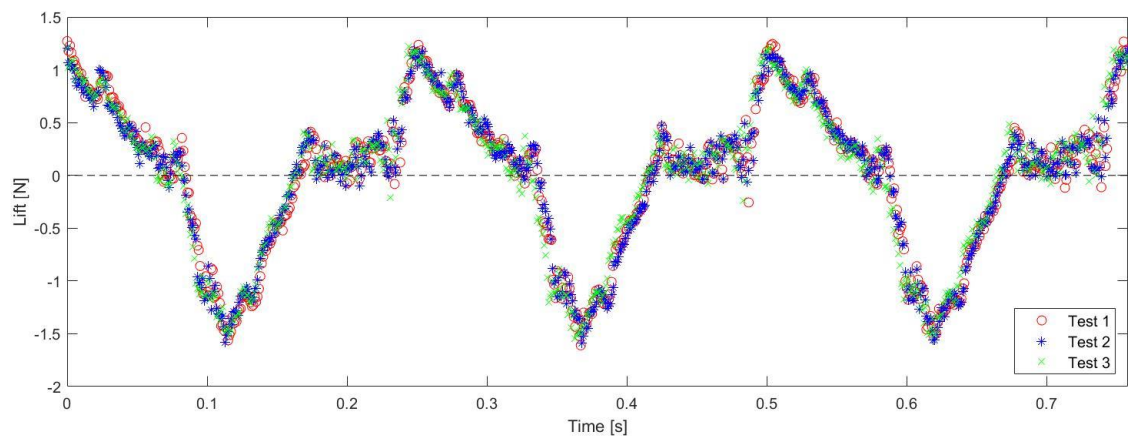


Figure 26: Lift at 4Hz when both wings are fixed

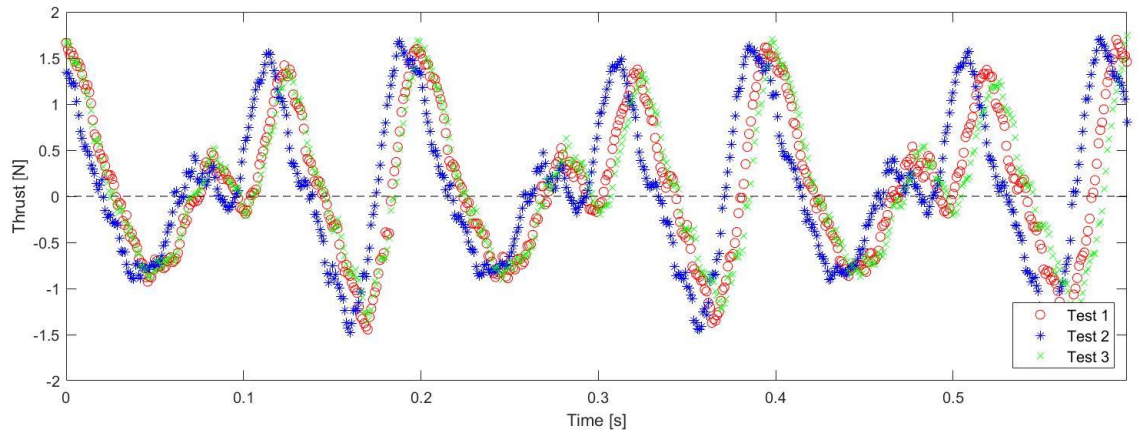


Figure 27: Thrust at 5Hz when both wings are fixed

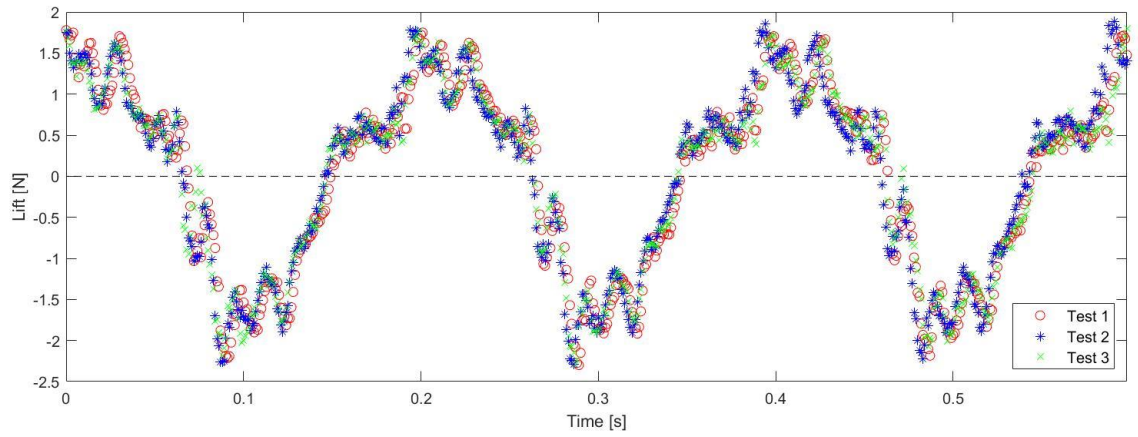


Figure 28: Lift at 5Hz when both wings are fixed

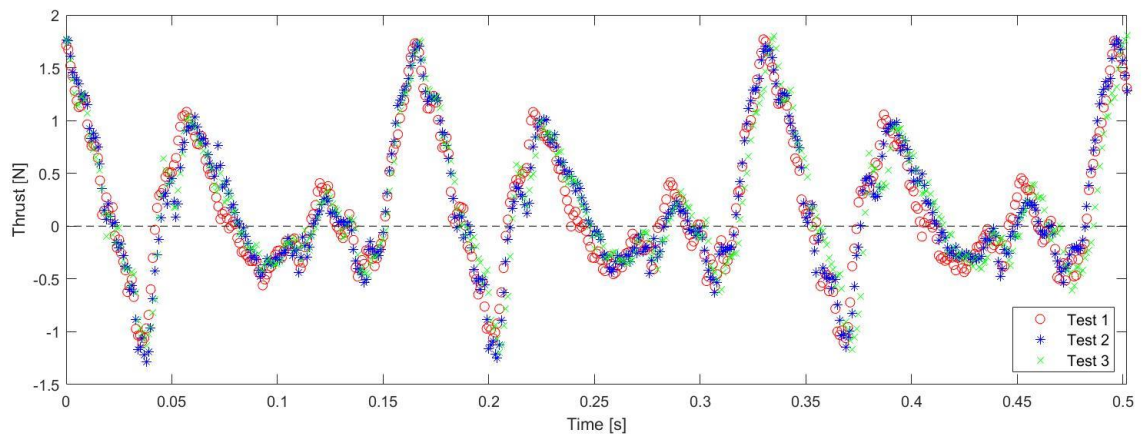


Figure 29: Thrust at 6Hz when both wings are fixed

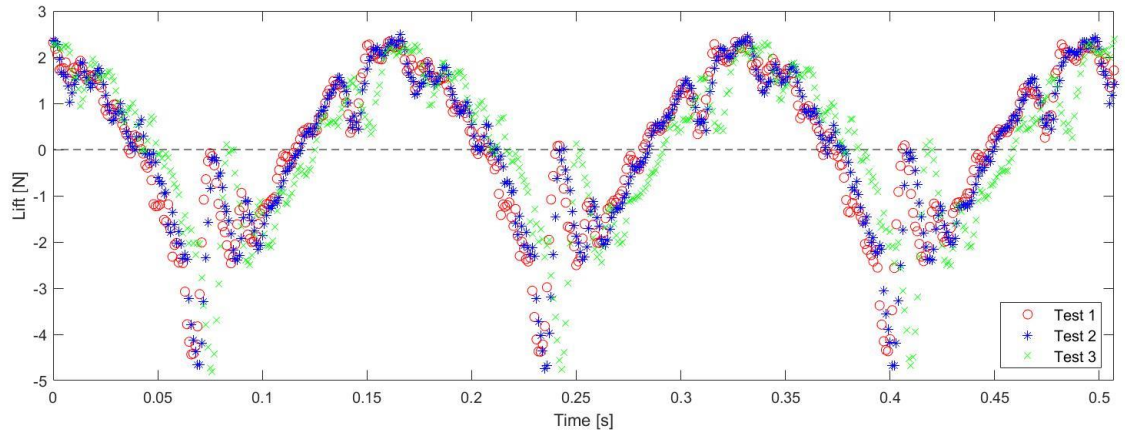


Figure 30: Lift at 6Hz when both wings are fixed

Table 6: Thrust and lift generated by B2 with fixed wings

Force	Frequency	Test 1	Test 2	Test 3	Average
Thrust	3 Hz	0.0178 N	0.0208 N	0.0174N	0.0186 N
	4 Hz	0.0367 N	0.0402 N	0.0430 N	0.0400 N
	5 Hz	0.0973N	0.1028 N	0.0923 N	0.0975 N
	6 Hz	0.1826 N	0.1885 N	0.1887 N	0.1866 N
Lift	3 Hz	0.0024 N	0.0030 N	0.0028 N	0.0027 N
	4 Hz	0.0019 N	0.0032 N	0.0050 N	0.0034 N
	5 Hz	0.0002 N	0.0098 N	0.0128 N	0.0076 N
	6 Hz	0.0070 N	0.0171 N	0.0145 N	0.0129 N

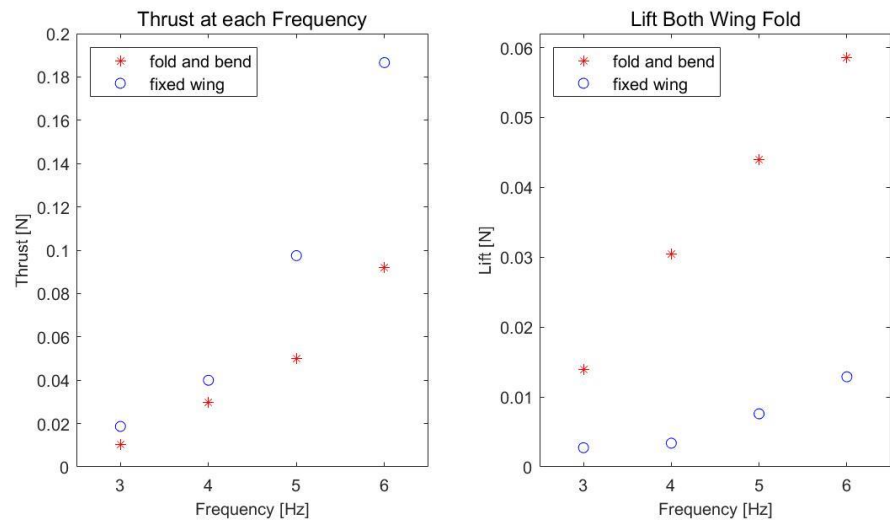


Figure 31: Thrust and lift at each frequency of fixed and folding wings

In the last load cell experiment, the right wing was fixed, while the left wing bent and folded during the upstroke. This test was performed at 6Hz only. In this case, the lift that was generated needed to differ between the two wing sides to allow a turning maneuver to be performed. According to the previous test, the folding left wing was supposed to create more lift than the fixed right wing, which would result in a positive roll moment around the body axis, thus allowing B2 to roll to the right side.

As in the previous experiment, three tests were run consecutively, and the test results were averaged. The roll moments for these three tests were  $0.0038 \text{ Nm}$ ,  $0.0029 \text{ Nm}$ , and  $0.0030 \text{ Nm}$ , respectively. The roll moments of all tests were positive as expected, and the average roll moment was  $0.0032 \text{ Nm}$ . When both wings were fixed during the test, the average roll moment was nearly  $0 \text{ Nm}$ , as indicated in Table 7. This finding evidences that folding and unfolding the left wing while the right wing remains fixed can allow bats to roll to the right. When both wings folded during the upstroke, the roll moments of all tests were negative, and the average roll moment was  $-0.0032 \text{ Nm}$ , which indicates that B2 rolled to left. This result was unexpected, as the motions of both wings are synchronous and should generate equal lift. All three tests reflect similar results, which could be due to the experimental setting or the wing structure itself. However, the subsequent flight test revealed the issue.

Table 7: Roll and yaw moment

Torque	Wing Structure	Test 1	Test 2	Test 3	Average
Roll	Fixed	-0.0012 Nm	0 Nm	-0.0001 Nm	-0.0004 Nm
	Folding	-0.0023 Nm	-0.0031 Nm	-0.0028 Nm	-0.0027 Nm
	Turning	0.0038 Nm	0.0029 Nm	0.0030 Nm	0.0032 Nm

## 4.2 Flight Test

The load cell test validated that the new wing structure of B2 was able to generate significantly more lift than the fixed wing at the cost of slightly reduced thrust. In the next step, B2 was tested in an open-loop flight experiment to check whether the new wing structure could provide adequate stability during the flight. Since no control system was needed for the open-loop flight, most onboard avionics were removed from B2. Only the electronic speed controller and the receiver were needed. A Spektrum DX8 transmitter was used to send signals to the receiver. The flight experiment was conducted in the indoor drone arena of the University of Illinois, Urbana-Champaign (see Figure 32) with a motion-capture volume of  $10 \cdot 9 \cdot 4 \text{ m}^3$  and a safety net. Eight Vicon T40 motion-capture cameras covered the motion capture volume and were able to run at 370 frames per second with full-frame resolution. Flight test data were collected at the frequency of 100Hz.



Figure 32 [36]: Indoor drone arena at the University of Illinois, Urbana-Champaign

Before the flight, B2 was mounted on a launcher with a rubber band and fixed by a trigger. When the trigger was released, B2 was ejected by the resilience of the rubber band. Several



straight flight test and turning flights were conducted. The first seven tests were straight flight tests with a synchronous flapping and folding movement of both wings. B2 was mounted on the launcher with an initial pitch angle of  $15^\circ$ . B2 was launched by releasing the trigger once it had reached a desired flapping frequency. In the first four straight flight tests, the legs and tail were on almost the same plane. In the next three tests, the legs were moved slightly upward such that the angle between the legs and the body plane was about  $20^\circ$ . Figure 33 visualizes the trajectories of all seven straight flight tests on the x-y-plane. The flight tests with the same leg setting clearly have highly similar results. In the first four flights, B2 maintained a straight flight for about 5 m after the flight had been launched. Then, it turned slightly to the left until the end of the flight, which implies that the lift and thrust that were generated were different between the two wing sides. This result is consistent with the outcome of the load cell test, which evidenced that the roll moment was negative when both wings folded and unfolded during the flight. Hence, the issue that was noted in previous section does not concern the experimental setting of the load cell test. Moreover, since the roll moment was nearly 0 Nm when both wings were fixed, an unsymmetrical flapping movement was not the problem either.

One reason for the unequal aerodynamic force between the two wings could be an asymmetry of the wings. Although B2 was assembled according to the CAD design, the structure could not be exactly the same as the designed one, as the carbon fiber rods were cut by hand and, hence, the precision of their length could not be ensured. Furthermore, the wing motions on the two sides were probably not symmetric. Although the new wing structure has only one DOA, and all other DOFs were passively determined by the motion of the spindle drive according to the theoretical design, the bending of the distal part of the

wing might have been caused by inertia or the weight of the wing itself if the screw was not tightened. During the downstroke, the proximal part of the wing flapped quickly downward, as it was directly connected to the crank by a ball-and-socket joint. The downstroke motion of the distal part of the wing was slower than the proximal part to allow the distal part of the wing to bend upward during the downstroke. Furthermore, the tensile force in the membrane could pull up the wing and prevent it from bending, which might be another factor that led to asymmetry of the wings. Therefore, perfectly symmetric motion of both sides of the wings could not be ensured during the flight. Tightening the screw might mitigate this issue, but B2 cannot bend its wings if the screws are too tight even though the proximal part of the wing can fold and unfold with the spindle drive motion. This issue was present in the open-loop flight test, but it could be solved in a closed-loop flight test wherein the control system is implemented to account for all of these external factors. After the legs were moved up to  $20^\circ$ , the trajectory became significantly straighter in the next three flight tests. No obvious turning could be observed in these three flight tests, which proves that the leg movement had the function of flight control in the robot bat flight.

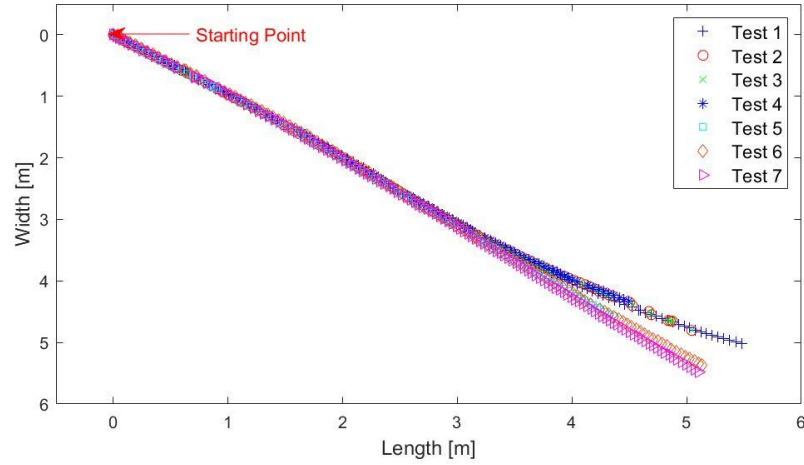


Figure 33: Trajectory of the straight flight data in the x-y-plane

To check B2's stability in these flight tests, the three Euler angles were calculated for all seven straight flight tests (see Figure 34). The Euler angles transformed the body frame into the inertial frame, which is located at the position of the launcher. The x- and y-axes of the inertial frame aligned with the border of the square flight arena, while the z-axis pointed upward. The body frame was located at the center of mass of B2. The x-axis pointed toward B2's head, while the y-axis pointed to the right side, and the z-axis pointed downward from the body. The transformation matrix from the body frame to the inertial frame was  $R_x(\pi)R_z(q_z)R_y(q_y)R_x(q_x)$ , where  $q_x$ ,  $q_y$ , and  $q_z$  are the roll, pitch, and yaw Euler angle.  $R_x(\pi)$  was multiplied by all other matrices since the z-axis of the inertial frame pointed upward, while the z-axis of the body frame pointed downward. As indicated in Figure 34, all Euler angles of these tests were within certain boundaries.  $q_x$  and  $q_y$  were mostly between  $-20^\circ$  and  $20^\circ$ . Since B2 was always launched in the diagonal direction in the flight arena,  $q_z$  was consistently around  $45^\circ$ .  $q_z$  should remain constant in a straight flight and gradually increase or decrease with time in a turning flight. As Figure 34



illustrates,  $q_z$  dropped from  $45^\circ$  to  $20^\circ$  in the second half of the first four flight tests, which indicates that B2 turned gradually to left at the end of these flights. In the next three flight tests,  $q_z$  remained around  $45^\circ$  throughout the flight despite some fluctuation at the beginning of the flight. Therefore, the last three flights were straighter than the first four as a result of the modified leg angles, which balanced the thrust and lift that were generated by both wings. Hence, the information that is provided by the trajectories in Figure 33 and by the yaw angles in Figure 34 are in agreement with each other.

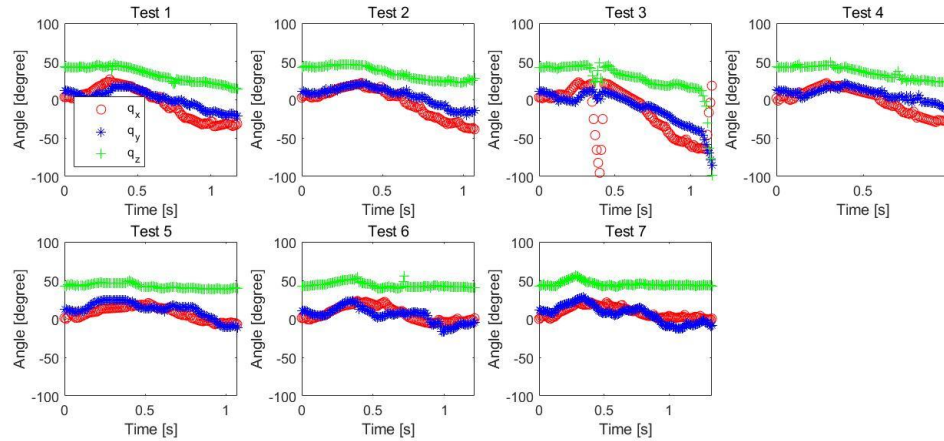


Figure 34: Euler angles of all straight flight tests

While the yaw Euler angle dropped from  $45^\circ$  to about  $20^\circ$  in the first four flight tests, the roll Euler angle also fell to  $-40^\circ$  in the second half of these tests. This finding reinforces that the right wing generated more lift than the left wing, which caused B2 to roll to the left and make a slight left turn even though the flapping and folding movements of both wings were synchronous. The reason is probably the asymmetry of the wings during the construction as well as the unexpected upward bending during the downstroke. In the next

three flight tests with a higher leg angle, there was no constant increasing and decreasing in the roll Euler angle, though some oscillation was observed. B2 did not roll onto one side continuously, and no turning flight was performed.

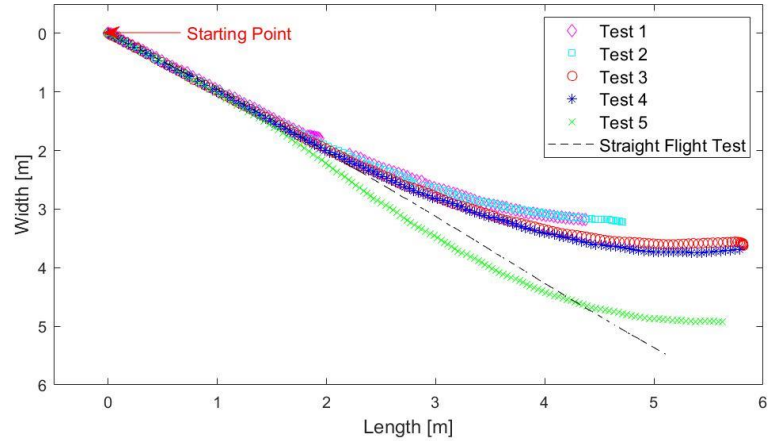


Figure 35: Trajectory of the turning flight data in the x-y plane

In the next step, B2 underwent five turning flight tests. In the turning flight, the left wing of B2 was fixed, while the right wing folded and bended during the upstroke. The right wing was expected to generate more lift than the left wing, which would cause B2 to roll to the left and make a left turn. The trajectories of all five turning flight tests on the x-y plane are visible in Figure 35. The launching angle of the first two tests were  $15^\circ$ , and that of the last three tests was  $20^\circ$ . Tests 4 and 5 involved more launching power than tests 1 through 3. This figure also includes the trajectory of the sixth straight flight test for comparison. As Figure 35 demonstrates, all of these flight tests presented a clear turning trajectory after B2 was launched. In tests 1 through 4, B2 started to turn immediately after launch. Although B2 turned slightly to the right at the beginning of the flight in test 5, it quickly modified the flight direction afterward and made a left turn. Therefore, B2 was

able to perform a turning maneuver through asynchronous motion of the left and right wing. B2 flew farther in tests 3 through 5 than in the first two tests since the initial pitch angle was higher in test last three tests. Therefore, lift generation in the turning maneuver was more difficult than in the straight flight, and B2 lost its height quickly since only the right wing could produce enough lift.

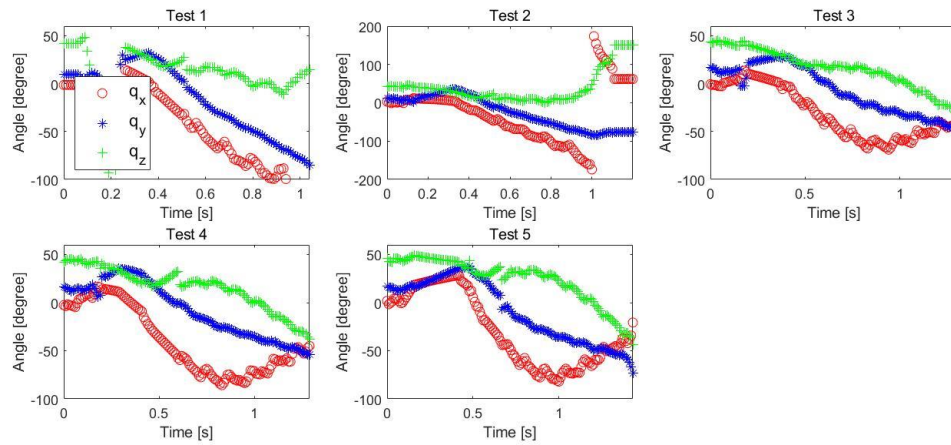


Figure 36: Euler angles of three turning flight tests

The Euler angles in Figure 36 also reveal that B2 made a left turn in all of these flight tests. The pitch Euler angle in tests 1 and 2 reflect that B2 dropped down into the nets with its head almost straight downward, as the pitch Euler angle reached around  $-80^\circ$  at the end of the flight. It again conveys that the lift generation in these tests was insufficient. After the launching angle was increased to  $20^\circ$ , B2 achieved improved flight performance. The yaw Euler angle dropped constantly from  $45^\circ$  to  $-40^\circ$ , which signifies that B2 changed its flight direction by almost  $90^\circ$ . The roll Euler angle was constantly negative at the same time, which indicates that B2 rolled to left to make a banked turn throughout the duration of the flight. Folding one side of the wing while keeping the other outstretched can help B2

complete a turning maneuver, but B2 is not able to generate adequate lift in this way. Although B2's pitch Euler angle increased up to about  $40^\circ$  due to the high initial launching angle shortly after it was launched, it dropped quickly to about  $-40^\circ$  throughout the flight. Nevertheless, the turning flight can be more accurately observed from the trajectories and the Euler angles in the last three tests. In future work, B2 still needs to generate more lift in order to maintain its height and achieve a longer flight.

## Chapter 5

### CONCLUSION

This thesis has proposed a new design for B2's wing structure. In addition to the three DOFs on each wing in the previous design, B2 can now bend the distal part of its wing during the upstroke. All four DOFs on the wing are passive and controlled by the linear motion of the spindle driver. B2 underwent several tests, including load cell tests and flight experiments. The result of the load cell tests support that the new wing structure with a bending motion was able to produce significantly more lift than thrust. Although the bending wings reduced the thrust by about 50%, lift is currently more crucial to overcome the weight of B2 itself. Furthermore, the test results reveal that increasing the flapping frequency could increase both lift and thrust. A bat is capable of flapping at a maximum frequency of about 10Hz, while B2's flapping frequency can reach up to about 8Hz. Since the motion of the distal part of the wing is always slower than that of the proximal part, the distal part oscillated with a small amplitude when it could no longer catch up with the high flapping frequency of the proximal part. As a result, both the lift and thrust that were generated by B2 decreased. The reason for this outcome may be that B2's wing reached its second or higher natural frequency so that the whole wing would not oscillate in the same direction spanwise. Future work should improve this aspect in order to make B2 flap at a higher frequency and produce more lift and thrust.

As the flight tests evidence, B2 could perform a straight flight in an open-loop flight test. Although the wing motion on the two sides was not perfectly symmetric, the leg movement was able to improve stability during the flight. Moreover, the downward bending of the distal part of the wing during the upstroke was able to generate more lift. However, the

distal part of the wing sometimes bent upward during the downstroke since not every part of the wing was rigid enough. As a result, the wing could not extend to its maximum span length during the downstroke. Solving this problem in the future will permit more lift and thrust production.

B2 also successfully completed a turning maneuver by folding and unfolding one side of its wing while keeping the other side fixed. In this way, the fixed side generated less lift, which caused B2 to roll onto that side and perform a turning flight. However, B2 was not able to maintain its height well in the turning flight, as the total lift that was generated by both wings was lower in that turning flight. If future adjustments can achieve a higher flapping frequency and improved bending structure, then B2 may be able to generate more lift to improve its flight performance.

## REFERENCES

- [1] J. Yu, M. Tan, S. Wang and E. Chen, "Development of a Biomimetic Robotic Fish and Its Control Algorithm," *IEEE Transactions on Systems Man, and Cybernetics, Part B (Cybernetics)* 34.4, pp. 1798-1810, 2004.
- [2] C. Menon, M. Murphy and M. Sitti, "Gecko Inspired Surface Climbing Robots," in *2004 IEEE International Conference on Robotics and Biomimetics*, 2004.
- [3] M. Dana, "A Flapping of Wings," pp. 1430-1433, 2012.
- [4] R. Zbikowski, C. Galinski and C. B. Pedersen, "Four-bar Linkage Mechanism for Insectlike Flapping Wings in Hover: Concept and an Outline of Its Realization," *J. Mech. Des.* 127.4, pp. 817-824, 2005.
- [5] T. Zhang, C. Zhou, C. Wang and X. Zhang, "Flapping Wing Mechanism Design Based on Mechanical Creative Design Theory," in *2011 International Conference on Mechatronic Science, Electric Engineering and Computer (MEC)*, 2011.
- [6] A. Ramezani, X. Shi, S.-J. Chung and S. Hutchinson, "Bat Bot (B2), A Biologically Inspired Flying Machine," in *2016 IEEE International Conference on Robotics and Automation (ICRA)*, 2016.
- [7] J. Hoff, A. Ramezani, S.-J. Chung and S. Hutchinson, "Optimizing the Structure and Movement of a Robotic Bat with Biological Kinematic Synergies," *The International Journal of Robotics Research* 37.10, pp. 1233-1252, 2018.
- [8] D. K. Riskin, D. J. Willis, T. L. Hedrick and I.-D. José, "Quantifying the complexity of bat wing kinematics," *Journal of Theoretical Biology* 254.3, pp. 604-615, 2008.
- [9] U. M. Norberg, "Aerodynamics, kinematics, and energetics of horizontal flapping flight in the long-eared bat *Plecotus auritus*," *Journal of Experimental Biology* 65.1, pp. 179-212, 1976.
- [10] I.-D. José, D. K. Riskin, D. J. Willis, K. S. Breuer and S. M. Swartz, "Whole-body Kinematics of a Fruit Bat Reveal the Influence of Wing Inertia on Body Accelerations," *Journal of Experimental Biology* 214.9, pp. 1546-1553, 2011.
- [11] I.-D. José and S. M. Swartz, "Kinematics of Slow Turn Maneuvering in the Fruit Bat *Cynopterus Brachyotis*," *Journal of Experimental Biology* 211.21, pp. 3478-3489, 2008.

- [12] J. W. Bahlman, Sharon M. Swartz and Kenneth S. Breuer, "Design and characterization of a multi-articulated robotic bat wing," *Bioinspiration & biomimetics* 8.1, p. 016009, 2013.
- [13] Y. Yu and Z. Guan, "Learning from Bat: Aerodynamics of Actively Morphing Wing," *Theoretical and Applied Mechanics Letters* 5.1, pp. 13-15, 2015.
- [14] A. Hedenström and L. C. Johansson, "Bat Flight: Aerodynamics, Kinematics and Flight Morphology," *Journal of Experimental Biology* 218.5, pp. 653-663, 2015.
- [15] J. D. Gardiner, G. Dimitriadis, J. R. Codd and R. L. Nudds, "A Potential Role for Bat Tail Membranes in Flight Control," *Plos One* 6.3, p. e18214, 2011.
- [16] U. M. Norberg, "Bat Wing Structures Important for Aerodynamics and Rigidity (Mammalia, Chiroptera)," *Zeitschrift für Morphologie der Tiere* 73.1, pp. 45-61, 1972.
- [17] M. Wolf, L. C. Johansson, Rhea von Busse, Y. Winter and A. Hedenström, "Kinematics of Flight and the Relationship to the Vortex Wake of a Pallas' Long Tongued Bat (*Glossophaga Soricina*)," *Journal of Experimental Biology* 213.12, pp. 2142-2153, 210.
- [18] F. T. Muijres, L. C. Johansson, Y. Winter and A. Hedenström, "Leading Edge Vortices in Lesser Long-nosed Bats Occuring at Slow But Not Fast Flight Speeds," *Bioinspiration & Biomimetics* 9.2, p. 025006, 2014.
- [19] D. K. Riskin, A. Bergou, K. S. Breuer and S. M. Swartz, "Upstroke Wing Flexion and the Inertial Cost of Bat Flight," *Proceedings of the Royal Society B: Biological Sciences* 279.1740, pp. 2945-2950, 2012.
- [20] S. M. Swartz, I.-D. José, D. K. Riskin and K. S. Breuer, "A Bird? A Plane? No, It's a Bat: An Introduction to the Biomechanics of Bat Flight," *Evolutionary History of Bats: Fossils, Molecules, and Morphology*, pp. 317-352, 2012.
- [21] Z.-W. Guan and Yong-liang Yu, "Aerodynamic mechanism of forces generated by twisting model-wing," *Applied Mathematics and Mechanics* 35.12, pp. 1607-1618, 2014.
- [22] J. A. Cheney, D. Ton, N. Konow, D. K. Riskin, K. S. Breuer and S. M. Swartz, "Hindlimb Motion During Steady Flight of the Lesser Dog-faced Fruit Bat, *Cynopterus Brachyotis*," *PloS One* 9.5, p. e98093, 2014.



- [23] U. M. L. Norberg and Y. Winter, "Wing Beat Kinematics of a Nectar-feeding Bat, *Glossophaga Soricina*, Flying at Different Flight Speeds and Strouhal Numbers," *Journal of Experimental Biology* 209.19, pp. 3887-3897, 2006.
- [24] M. R. A. Nabawy and W. J. Crowther, "The Role of the Leading Edge Vortex in Lift Augmentation of Steadily Revolving Wings: A Change in Perspective," *Journal of the Royal Society Interface* 14.132, p. 20170159, 2017.
- [25] S. P. Sane, "The aerodynamics of insect flight," *Journal of experimental biology* 206.23, pp. 4191-4208, 2003.
- [26] I. Gursul, Z. Wang and E. Vardaki, "Review of Flow Control Mechanisms of Leading-edge Vortices," *Progress in Aerospace Sciences* 43.7-8, pp. 246-270, 2007.
- [27] F. T. Muijres, L. C. Johansson, R. Barfield, M. Wolf, G. R. Spedding and A. Hedenström, "Leading-Edge Vortex Improves Lift in Slow-Flying Bats," *Science* 319.5867, pp. 1250-1253, 2008.
- [28] G. Koekkoek, F. T. Muijres, L. C. Johansson, M. Stuijver, B. W. van Oudheusden and A. Hedenström, "Stroke Plane Angle Controls Leading Edge Vortex in a Bat-inspired Flapper," *Comptes Rendus Mecanique* 340.1-2, pp. 95-106, 2012.
- [29] H. D. J. N. Aldridge, "Vertical Flight in the Greater Horseshoe Bat *Rhinolophus Ferrumequinum*," *Journal of Experimental Biology* 157.1, pp. 183-204, 1991.
- [30] H. D. J. N. Aldridge, "Body Accelerations During the Wingbeat in Six Bat Species: The Function of the Upstroke in Thrust Generation," *Journal of Experimental Biology* 130.1, pp. 275-293, 1987.
- [31] H. D. J. N. Aldridge, "Turning Flight of Bats," *Journal of Experimental Biology* 128.1, pp. 419-425, 1987.
- [32] U. M. Norberg, "Some Advanced Flight Manoeuvres of Bats," *Journal of Experimental Biology* 64.2, pp. 489-495, 1976.
- [33] X. Tian, J. Iriarte-Diaz, K. Middleton, R. Galvao, E. Israeli, A. Roemer, A. Sullivan, A. Song, S. Swartz and K. Breuer, "Direct Measurements of the Kinematics and Dynamics of Bat Flight," *Bioinspiration & Biomimetics* 1.4, p. S10, 2006.
- [34] J. M. V. Rayner and H. D. J. N. Aldridge, "Three-Dimensional Reconstruction of Animal Flight Paths and the Turing Flight of Microchiropteran Bats," *Journal of Experimental Biology* 118.1, pp. 247-265, 1985.

- [35] FESTO, "BionicFlyingFox," 2018. [Online]. [Accessed 20 Jan 2020].
- [36] ILLINOIS ROBOTICS GROUP, "Lab Manual," [Online]. Available: <https://robotics.illinois.edu/lab-manual/>. [Accessed 3 March 2020].
- [37] R. Von Busse, A. Hedenström, Y. Winter and L. C. Johansson, "Kinematics and Wing Shape Across Flight Speed in the Bat, *Leptonycteris Yerbabuenae*," *Biology Open* 1.12, pp. 1226-1238, 2012.
- [38] R. Dudley, "Mechanisms and Implications of Animal Flight Maneuverability," *Integrative and Comparative Biology* 42.1, pp. 135-140, 2002.